The Non-universal Pseudo Phase-Space Density Profiles of Symphony Host Halos

Bocheng Feng¹*,Ethan O. Nadler²†, S. Peng Oh³, and Suoqing Ji^{4,5}

25 November 2025

ABSTRACT

Cosmological N-body simulations have long suggested that the pseudo phase-space density (PPSD), ρ/σ^3 , of cold dark matter halos follows the universal relation $\rho/\sigma^3 \propto r^\chi$, with $\chi \approx -1.875$, as predicted by spherical secondary-infall similarity solutions. This power law appears to hold despite the fact that neither the density $\rho(r)$ nor velocity dispersion $\sigma(r)$ follow universal power law relations individually, even at fixed mass. We analyze 246 host halos from the *Symphony* suite of high-resolution cosmological zoom-in simulations, to consistently measure PPSD profiles across host masses from 10^{11} to $10^{15} M_{\odot}$. We find that the PPSD systematically deviates from a power law, and that halos with larger deviations from Jeans equilibrium systematically develop steeper average PPSD slopes. This result suggests that the PPSD is not universal; instead, it is linked to a halo's degree of dynamical equilibrium, which is ultimately set by halo formation history. As a result, we show that secondary halo properties such as concentration and accretion rate inherit significant correlations with the PPSD slope. Moreover, our hosts' PPSD profiles are remarkably consistent with predictions from 1D self-similar fluid collapse models, indicating that three-dimensional structure, velocity anisotropy, and cosmological environment all play negligible roles in shaping the PPSD. These findings imply that the PPSD does not follow a universal power law, but is instead determined by halo mass assembly history alone.

Key words: cosmology: dark matter – galaxies: halos – galaxies: structure – galaxies: kinematics and dynamics

1 INTRODUCTION

The inner structure of dark matter halos is a key prediction of the cold dark matter (CDM) paradigm. In the standard cosmological picture, halos form through hierarchical gravitational collapse, continuously growing via mergers and the smooth accretion of surrounding material. Despite the complexity of this process, cosmological N-body simulations reveal that halos share remarkably similar internal structures (Press & Schechter 1974; White & Rees 1978; Huss et al. 1999; van den Bosch 2002). Cosmological N-body simulations show that the spherically averaged density profiles of halos are well described by simple functional forms such as the Navarro-Frenk-White (NFW; Navarro et al. 1996; Navarro et al. 1997) or Einasto profiles (Einasto 1965), exhibiting only mild variations across halo mass and redshift (Dalal et al. 2010; Hjorth et al. 2015; Wang et al. 2020). This structural similarity has motivated extensive efforts to understand the physics governing the emergence of universal halo structure (e.g., see Zavala & Frenk 2019 for a review).

Beyond their spatial structure, dark matter halos also display unexpected universality in phase space. A particularly striking aspect of halo dynamics is the so-called pseudo phase-space density profile (PPSD; Taylor & Navarro 2001), defined as

$$Q(r) \equiv \rho(r)/\sigma^{3}(r),\tag{1}$$

where ρ is the dark matter mass density and σ is the velocity dispersion. The PPSD connects spatial and kinematic structure: in collisionless systems, the fundamental invariant is the fine-grained phase-space density $f(\mathbf{x}, \mathbf{v})$, which is conserved according to Liouville's theorem (Binney & Tremaine 2008). Although f cannot be directly observed or measured in simulations, the PPSD serves as a coarse-grained proxy of the true phase-space density f and has been shown to trace the dominant structures in phase space (Maciejewski et al. 2009).

Early *N*-body simulations revealed that the PPSD is surprisingly universal: for simulated CDM halos, Q(r) follows apower law $Q(r) \propto r^{\chi}$, with $\chi \approx -1.875$, over 2 decades in radius and with very little variation across halos (Taylor & Navarro 2001; Dehnen & McLaughlin 2005; Navarro et al. 2010; Ludlow et al. 2010a, 2011; Colombi 2021). This behavior is particularly striking because neither $\rho(r)$ nor $\sigma(r)$ follow single power laws themselves, and both vary from halo to halo, even at fixed mass. The apparent universality of ρ/σ^3 therefore raises a fundamental question: what dynamical mechanism enforces this power-law behavior in collisionless, hierarchically growing systems? For example, does the PPSD point to

¹Department of Astronomy, School of Physics, Peking University, Beijing 100871, China

²Department of Astronomy & Astrophysics, University of California, San Diego, La Jolla, CA 92093, USA

³Department of Physics, University of California, Santa Barbara, Santa Barbara, CA 93106, USA

⁴Center for Astronomy and Astrophysics and Department of Physics, Fudan University, Shanghai 200438, China

⁵Key Laboratory of Nuclear Physics and Ion-Beam Application (MOE), Fudan University, Shanghai 200433, P.R.China

bochengfeng.phy@stu.pku.edu.cn

enadler@ucsd.edu

an additional integral of motion for self-gravitating systems, or is it simply an emergent coincidence?

The puzzle deepens when considering that the measured slope $\chi \approx -1.875$ matches the value predicted by self-similar secondary infall (Bertschinger 1985; Williams et al. 2005), an idealized model describing the collapse of matter onto a point mass in an Einstein–de Sitter universe (Bertschinger 1985; Williams et al. 2005). Real halos, however, assemble through mergers (Cole et al. 2008), develop triaxial shapes (Allgood et al. 2006), and exhibit anisotropic velocity distributions (Hansen & Moore 2006), none of which resemble the assumptions of the self-similar model. Why such a simplified analytic model reproduces the PPSD scaling observed in full cosmological simulations remains one of the most intriguing open questions in halo dynamics.

Beyond its theoretical importance, the PPSD has also been invoked as an observational diagnostic of the innermost density profiles of CDM halos. If Q(r) indeed follows a nearly universal power law, then empirical determinations of $\sigma(r)$ —from stellar dynamics in galaxies, globular cluster kinematics, or distortions in strong-lensing arcs—can be used to infer the underlying density profile by extrapolating. On group and cluster scales, joint analyses that combine dark matter kinematics with the thermodynamic properties of the baryonic gas have probed the PPSD (Pratt et al. 2006; Voit 2005; Cavagnolo et al. 2009b; Capasso et al. 2018). For instance, Faltenbacher et al. (2007) demonstrated that the radial PPSD and entropy profiles inferred for galaxy clusters are consistent with power laws and exhibit comparable slopes. More recently, Biviano & Mamon (2023) analyzed the kinematics of 54 WINGS clusters and found that their inferred PPSD profiles are consistent with an approximate powerlaw, providing observational support for the numerical prediction.

Despite these motivations, a growing body of work also challenges the strict universality of the PPSD (Williams et al. 2005; Ludlow et al. 2010a, 2011; Popolo 2011; Nadler et al. 2017; Arora & Williams 2020). Using one-dimensional fluid simulations, Nadler et al. (2017) argued that deviations from equilibrium, which could arise from recent accretion or incomplete virialization, naturally produce departures from the $\chi \approx -1.875$ power law. Meanwhile, Arora & Williams (2020) showed that power-law PPSD solutions are generally incompatible with the structure of the Jeans equation for dynamically relaxed systems. However, these lines of argument are idealized; they both invoke spherical symmetry, and additionally assume either the fluid approximation or dynamical equilibrium. In contrast, cosmological halos grow within a rich, hierarchical phasespace environment (Ludlow et al. 2010b), and it remains unclear whether these idealized expectations for the PPSD carry over to realistic structure formation.

These issues highlight a fundamental gap in our understanding: despite decades of work, we still lack a cosmologically grounded explanation for why PPSD profiles follow a near-universal scaling—and under what conditions this behavior breaks down. This motivates a systematic reanalysis of PPSD structure using cosmological simulations that capture mergers, anisotropy, triaxiality, and the hierarchical growth. In this work, we therefore aim to quantify the degree of universality in the PPSD-both within individual halos and across the halo population—and to identify the physical processes that set its shape. To achieve this, we use the Symphony suite of high-resolution CDM zoom-in simulations spanning host halo masses from 10¹¹ to 10^{15} , M_{\odot} (Nadler et al. 2023). Because of its large dynamic range and uniform resolution, Symphony provides an ideal dataset for investigating how Q(r) depends on halo mass, assembly history, dynamical state, and secondary halo properties. By combining detailed measurements of density, velocity dispersion, and anisotropy profiles, we quantify deviations from Jeans equilibrium and show how these shape PPSD profiles.

This paper is organized as follows. In Section 2, we describe our zoom-in simulations and analysis techniques. In Section 3, we measure the density, velocity dispersion, velocity anisotropy, and PPSD profiles across *Symphony* suites. In Section 4, we study how deviations from Jeans equilibrium shape PPSD profiles, the redshift evolution of the PPSD, and correlations between secondary halo properties and PPSD slopes. In Section 5, we compare our PPSD results with the Nadler et al. (2017) 1D fluid simulations. In Section 6, we summarize our main results and discuss.

2 SYMPHONY SIMULATIONS AND ANALYSIS METHODS

We use 246 cosmological, CDM host halos in *Symphony* simulations, a compilation of five dark matter—only zoom-in suites:

- LMC-mass hosts ($10^{11} M_{\odot}$; the "LMC" suite);
- Milky Way-mass hosts ($10^{12} M_{\odot}$; the "Milky Way" suite);
- Group-mass hosts ($10^{13} M_{\odot}$; the "Group" suite);
- Low-mass cluster hosts $(4 \times 10^{14} M_{\odot})$; the "L-Cluster" suite);
- Cluster-mass hosts ($10^{15} M_{\odot}$; the "Cluster" suite)

Across the entire mass range, each host halo consists of more than 10^6 particles and the highest-resolution regions are resolved with a Plummer-equivalent gravitational softening length of $\approx 9 \times 10^{-4} R_{\rm vir}$, on average, where $R_{\rm vir}$ is the host halo virial radius. Below, we provide a brief summary of simulation parameters and our analysis techniques. More details about the *Symphony* simulations can be found in Nadler et al. (2023).

2.1 Cosmological parameters

The *Symphony* compilation adopts slightly different cosmological parameters across its five suites, reflecting the specifications of their parent simulations. The LMC, Milky-Way, and Group suites are drawn from a 1024^3 -particle, $125h^{-1}$ Mpc-box run in a flat Λ CDM cosmology with h=0.7, $\Omega_{\rm m}=0.286$, $\Omega_{\Lambda}=0.714$, $\sigma_8=0.82$, and $n_s=0.96$ (Hinshaw et al. 2013; Mao et al. 2015). These cosmological parameters correspond to a virial overdensity of $\Delta_{\rm vir}\simeq 99$ at z=0 (Bryan & Norman 1998).

The L-Cluster suite originates from a 1024^3 -particle, $1h^{-1}$ Gpc-box parent run with cosmological parameters h=0.7, $\Omega_{\rm m}=0.3$, $\Omega_{\Lambda}=0.7$, $\sigma_8=0.85$, and $n_s=0.96$, corresponding to $\Delta_{\rm vir}\simeq 101$ (Bhattacharyya et al. 2022).

Finally, the Cluster suite is based on the Carmen simulation (McBride et al. 2009) of side length $1h^{-1}$ Gpc with 1024^3 particles per side, which adopts cosmological parameters h=0.7, $\Omega_{\rm m}=0.25$, $\Omega_{\Lambda}=0.75$, $\sigma_{8}=0.8$, and $n_{s}=1.0$, corresponding to $\Delta_{\rm vir}\simeq 94$ at z=0 (Wu et al. 2013a,b). These small cosmological differences among suites do not impact our results but should be kept in mind for cross-suite comparisons.

Across the entire *Symphony* compilation, the particle mass scales approximately as $m_{\rm part} \simeq 3 \times 10^{-7} M_{\rm host}$, allowing well-resolved measurements of host density and kinematic profiles over four decades in host halo mass. The comoving Plummer-equivalent gravitational softening length is set to $\epsilon \simeq 9 \times 10^{-4} R_{\rm vir}$, on average, which avoids both artificial suppression of central densities from excessive softening and integration errors from insufficient softening (Nadler et al. 2023). We list the main properties of each suite in Table 1.

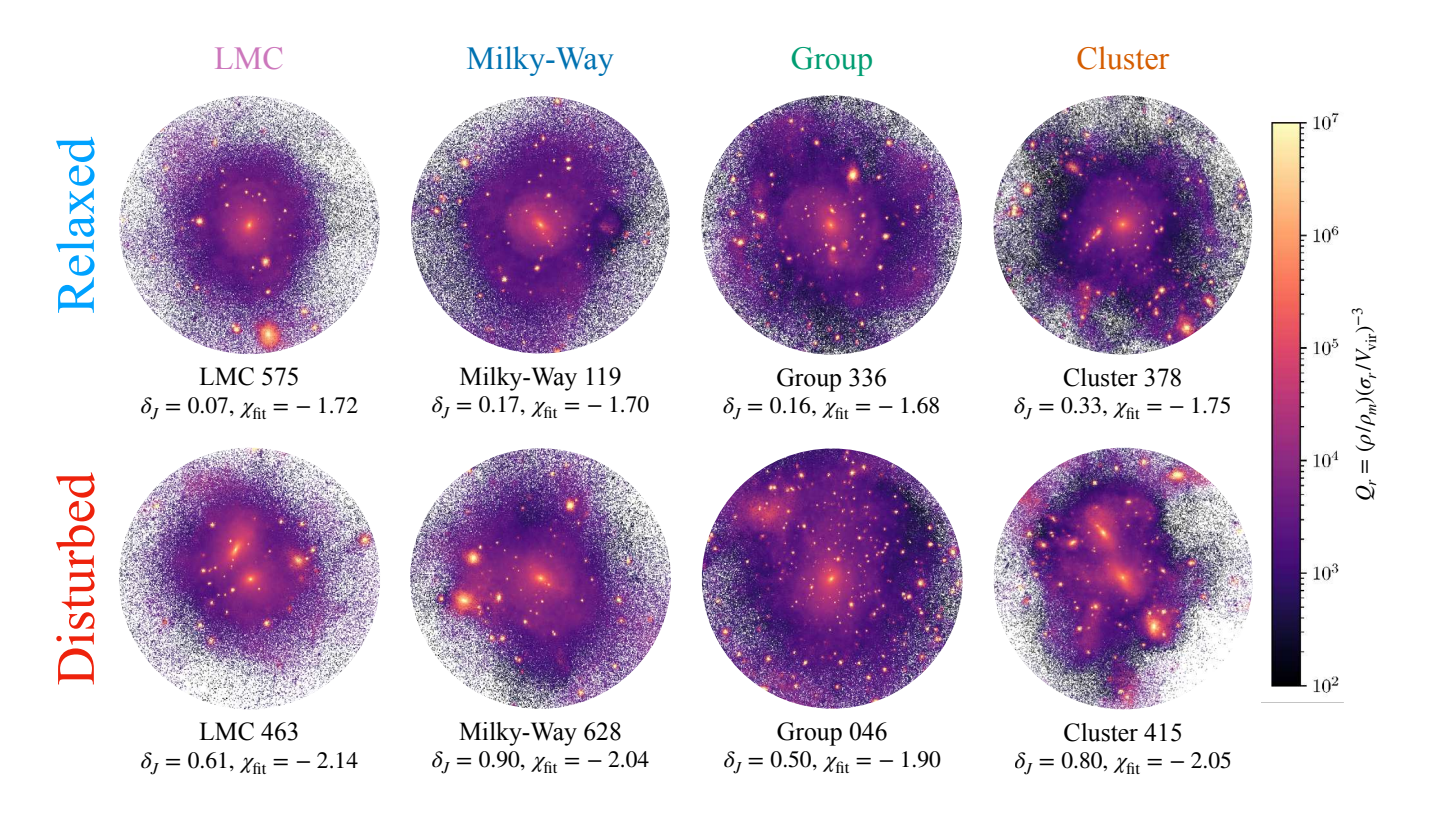


Figure 1. Projected radial pseudo phase-space density (PPSD) maps of representative host halos at z = 0 from the LMC, Milky-Way, Group, and Cluster suites in our simulations, shown across columns. The top row shows relaxed systems close to Jeans equilibrium, while the bottom row shows disturbed systems far from Jeans equilibrium in the corresponding suites. The departure from equilibrium is quantified by the Jeans deviation parameter δ_J (See Section 4.2 for details). For each host, the best-fit average radial PPSD slope, $\chi_{\rm fit}$, is also indicated in the corresponding panel. Each visualization is a slice of thickness $0.2R_{\rm vir}$ extending out to the virial radius.

Table 1. Numerical properties of the five *Symphony* suites. The first column lists the name of suite, the second column lists the number of zoom-in simulations we use, the third column lists the median and standard deviation of the host halo virial mass, the fourth column lists the dark matter particle mass in the highest-resolution zoom-in region, and the last column lists the comoving Plummer-equivalent force softening length. Note that we omit 16 simulations from the Cluster suite, relative to the 96 presented in Nadler et al. (2023), due to corrupted particle data.

Zoom-in Suite	$N_{\rm sim}$	$M_{ m host} (M_{\odot})$	$m_{\rm p} (M_\odot)$	$\epsilon \ (\mathrm{pc} \ h^{-1})$
LMC	39	$10^{11.02\pm0.05}$	5.0×10^{4}	80
Milky Way	45	$10^{12.09\pm0.02}$	4.0×10^{5}	170
Group	49	10 ^{13.12±0.11}	3.3×10^{6}	360
L-Cluster	33	10 ^{14.62±0.11}	2.2×10^{8}	1200
Cluster	80	$10^{14.96\pm0.03}$	1.8×10^{8}	325

2.2 Analysis Techniques

2.2.1 Density, Velocity and PPSD Profiles

To compute the profiles of the spherically averaged pseudo phase-space density (PPSD) as a function of radius, we divide each host halo into 40 logarithmically-spaced spherical shells spanning $10^{-3}R_{\rm vir}$ to $1.5R_{\rm vir}$, where $R_{\rm vir}$ denotes the virial radius of each host. The average density profile $\rho(r)$ in each bin is obtained by dividing the total mass within the shell by its volume. The radial velocity dispersion profile, $\sigma_{\rm rad}(r)$, is measured in the host rest frame as the average radial velocity dispersion of particles in each shell. Figure 1

shows examples of PPSD profiles in different suites across columns; we further illustrate dynamically "relaxed" versus "disturbed" halos within each suite in different rows. As we will show below, the magnitude of the deviation from Jeans equilibrium correlates with properties of the PPSD profiles.

The total velocity dispersion is defined as the quadratic sum of the dispersions in the three Cartesian components, $\sigma_{\text{tot}}^2 = \sigma_x^2 + \sigma_y^2 + \sigma_z^2$, which is equivalent to twice the specific kinetic energy. The velocity anisotropy parameter is then defined as

$$\beta(r) \equiv 1 - \frac{\sigma_{\text{tan}}^2(r)}{2\sigma_{\text{rad}}^2(r)},\tag{2}$$

where the tangential velocity dispersion is given by $\sigma_{\text{tan}}^2 = \sigma_{\text{tot}}^2 - \sigma_{\text{rad}}^2$. With this definition, $\beta = 0$ corresponds to an isotropic velocity distribution, while $\beta = 1$ describes purely radial orbits.

We consider both the total PPSD, defined as $Q_{\text{tot}}(r) \equiv \rho/\sigma_{\text{tot}}^3$, and the radial PPSD, $Q_r(r) \equiv \rho/\sigma_{\text{rad}}^3$. In the following analysis we focus primarily on $Q_r(r)$, since the radial velocity dispersion directly enters the Jeans equation. We demonstrate in Appendix A2 that the choice between Q_{tot} and Q_r does not affect our results.

2.2.2 PPSD slope smoothing

We compute smooth derivatives of the PPSD profiles using the pynumdiff package (van Breugel et al. 2020; van Breugel et al. 2022). In particular, we adopt the constant_jerk variant of the Kalman smoothing algorithm, which assumes a locally constant third

4 Feng & Nadler et al.

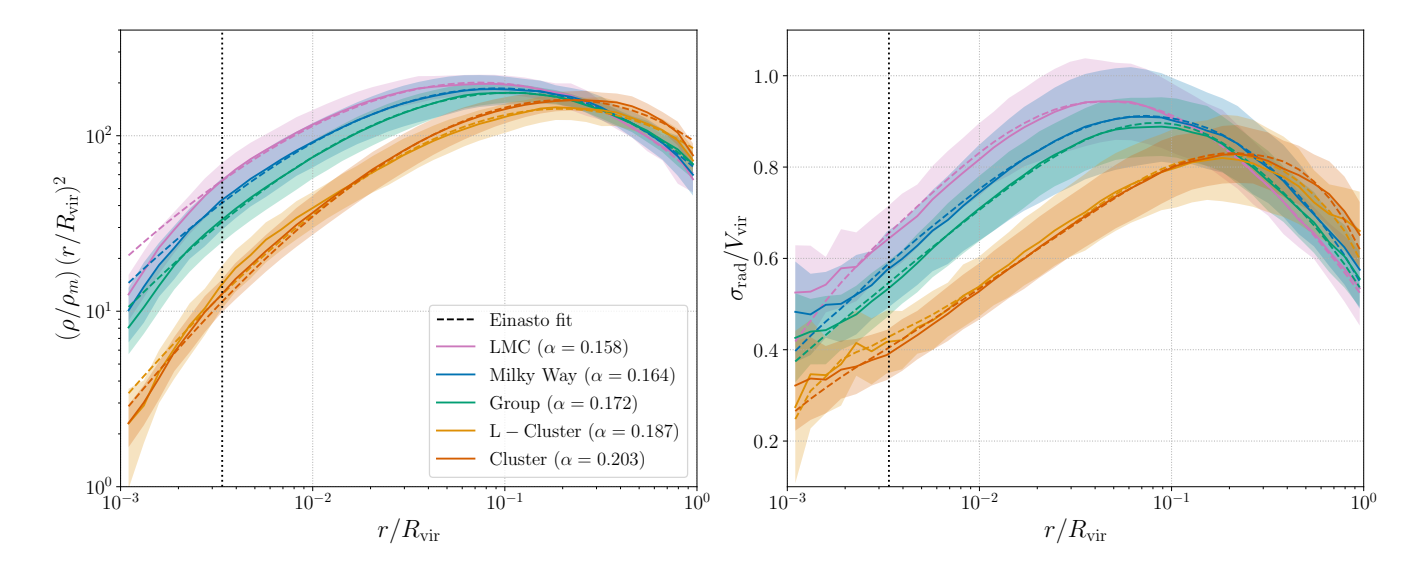


Figure 2. Density (left) and radial velocity dispersion (right) profiles of host halos in *Symphony* suites. Solid lines show suite averages, with radii scaled by $R_{\rm vir}$, densities scaled by ρ_m (the mean matter density at z=0), and velocity dispersions scaled by $v_{\rm vir}$ (the host virial velocity). Densities are multiplied by $(r/R_{\rm vir})^2$, to enhance the dynamic range. Dashed lines in the left panel show the best-fit Einasto density profiles, while dashed lines in the right panel are obtained by solving the Jeans equation for the corresponding Einasto models using the measured velocity anisotropy profiles. Shaded regions indicate the 68% halo-to-halo scatter within each suite. The dotted vertical line marks the most conservative convergence radius across suites, below which measurements may not be converged.

derivative (jerk) of the signal. As demonstrated in Appendix D, this method can reliably recover underlying power-law PPSD profiles within the radial range $6 \times 10^{-3} R_{\rm vir} - 1.1 R_{\rm vir}$. We therefore adopt this radial range when estimating best-fit average PPSD slopes, hereafter denoted as $\chi_{\rm fit}$.

To enable stacking of halo profiles across different mass scales, we normalize the radial coordinate by each host halo's virial radius, $r \to r/R_{\rm vir}$, the density by the mean matter density at z=0 in each suite, $\rho \to \rho/\rho_m$, and the velocity dispersion by each host halo's virial velocity, $\sigma \to \sigma/V_{\rm vir}$. Accordingly, the PPSD is expressed in units of $\rho_m/V_{\rm vir}^3$. In the following, all profiles and derived quantities are presented using this normalization unless stated otherwise. We also provide an empirical fit to the PPSD amplitude as a function of halo mass in Appendix A2.

3 SYMPHONY HOST HALO PROFILES

In this section, we present host halo density, velocity dispersion, velocity anisotropy and PPSD profiles. We discuss our main results in Section 4.

3.1 Density and velocity dispersion profiles

Figure 2 shows the mean density and radial velocity dispersion profiles (measured in the host rest frame) of host halos at z=0 in each simulation suite. The dotted line marks the "convergence radius," 2.8ϵ (Ludlow et al. 2019), shown here for the Cluster suite because it is the largest (and thus most conservative) convergence radius across all suites when expressed in units of $R_{\rm vir}$. Shaded regions denote the $\pm 1\sigma$ halo-to-halo scatter within each suite. For clarity, the density profiles are multiplied by r^2 , which highlights the radius where the logarithmic slope, $\gamma(r) \equiv {\rm d} \ln \rho(r)/{\rm d} \ln r$, reaches $\gamma = -2$.

In the left panel of Figure 2, the dashed lines represent fits of the

Einasto profile (Einasto 1965) to the mean density profiles of each suite. This three-parameter model is defined as

$$\ln\left(\frac{\rho}{\rho_{-2}}\right) = -\frac{2}{\alpha} \left[\left(\frac{r}{r_{-2}}\right)^{\alpha} - 1 \right],\tag{3}$$

where $\rho_{-2} \equiv \rho(r_{-2})$ and r_{-2} denote the density and radius at which the logarithmic slope equals -2, respectively. The shape parameter α controls the curvature of the density profile. As expected, the Einasto model provides a more accurate description of our host halos than the Navarro–Frenk–White (NFW; Navarro et al. 1996; Navarro et al. 1997) profile. In particular, the additional degree of freedom introduced by α is essential to capture the curvature in the measured density profiles, consistent with previous results (e.g. Navarro et al. 2004; Merritt et al. 2005, 2006; Gao et al. 2008; Hayashi & White 2008; Navarro et al. 2009; Ludlow et al. 2011). Furthermore, as shown in the left panel of Figure 2, the best-fit values of α systematically increase with host halo mass, and this trend becomes steeper at higher masses. Note that the inferred values of α for each suite are consistent with those reported in earlier studies (e.g. Ludlow et al. 2013; Dutton & Macciò 2014).

To provide a practical method for fitting velocity dispersion profiles, we also construct $\sigma_{\rm rad}$ predictions based on the Einasto density profile. In the right panel of Figure 2, the dashed lines show the velocity dispersion profiles constructed from the corresponding Einasto models in the left panel. These constructed profiles are obtained by solving the Jeans equation using the measured velocity anisotropy profiles for each suite, assuming an Einasto density profile. Velocity dispersion profiles also exhibit systematic variations in shape across the Symphony suites, and the Einasto-based solutions reproduce them accurately over the full range of host halo masses considered.

We assume that the velocity anisotropy goes to zero outside the virial radius when constructing these solutions.

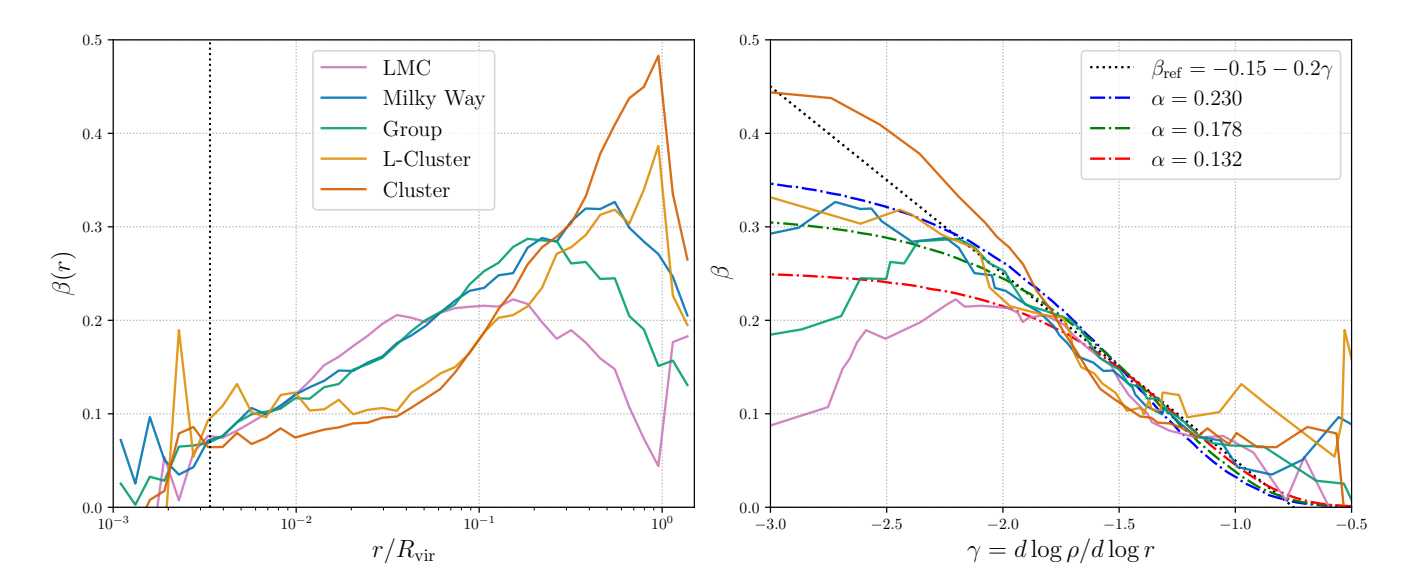


Figure 3. Left panel: Velocity anisotropy profiles of host halos in the Symphony suites at z=0. The dotted vertical line marks the most conservative convergence radius across all suites, below which measurements may not be converged. Right panel: Mean density slope-velocity anisotropy relation (Equation 4) for host halos in Symphony suites at z=0. The dotted line shows the linear relation proposed by Hansen & Moore (2006). The dot-dashed curves depict the model of Ludlow et al. (2011), given by Equation 5, assuming that $\gamma(r)$ follows an Einasto profile. Blue, green, and red dot-dashed lines correspond to $\alpha=0.230$, 0.178, and 0.132, respectively.

From Figure 2, it is apparent that the $r^2\rho(r)$ and $\sigma(r)$ profiles follow very similar radial trends. This similarity implies the existence of a simple scaling relation between the density and velocity dispersion profiles, which partly motivates the construction of the PPSD (e.g., see the discussion in Navarro et al. 2009).

3.2 Velocity anisotropy profiles

The left panel of Figure 3 shows the mean velocity anisotropy profiles for all simulation suites at z = 0, again as a function of $r/R_{\rm vir}$. We find that host halos in all suites have nearly isotropic velocity distributions in their central regions, typically with $\beta \lesssim 0.1$. The LMC, Milky Way, and Group suites exhibit similar overall shapes of the velocity anisotropy profile: $\beta(r)$ increases with radius, indicating a transition from isotropic orbits in the innermost regions to more radially biased orbits near the scale radius; their $\beta(r)$ profiles then decline again toward the outskirts, becoming more isotropic at large radii. The radius at which this transition occurs shows a systematic dependence on the suite mass: more massive hosts exhibit the transition at larger radii, and the peak value of β at this location also tends to increase with suite mass. In contrast, the L-Cluster and Cluster suites display somewhat different behavior: their $\beta(r)$ profiles do not exhibit a clear peak but instead increase monotonically with radius, until they decline sharply near the virial radius.

Hansen & Moore (2006) proposed that relaxed halos follow a nearly universal linear relation between the density slope and the velocity anisotropy (the β – γ relation), which can be expressed as

$$\beta(\gamma) = \eta_1 - \eta_2 \gamma,\tag{4}$$

where $-0.45 < \eta_1 < 0.05$ and $0.1 < \eta_2 < 0.35$. This empirical relation provides a closure condition for solving the Jeans equation in anisotropic systems. The right panel of Figure 3 shows the mean β - γ relations for all *Symphony* suites, along with the Hansen & Moore (2006) fit (dotted line). We find that the velocity anisotropy

in the inner regions of *Symphony* halos, where $\gamma > -2$, can be well approximated by a universal parameter combination of $\eta_1 = -0.15$ and $\eta_2 = 0.2$ within r_{-2} , the radius at which the density slope equals -2. However, at larger radii where $-3 < \gamma < -2$, the profiles systematically deviate from the linear relation. This suggests that the linear $\beta - \gamma$ relation provides a good description of the inner halo regions but breaks down in the outskirts, where halos are no longer fully relaxed.

Ludlow et al. (2011) further proposed that Equation 4 can be replaced by a more flexible form,

$$\beta(\gamma) = \frac{\beta_{\infty}}{2} \left[1 + \operatorname{erf}\left(\ln[(A\gamma)^2]\right) \right],\tag{5}$$

which better reproduces the behavior of the β - γ relation in the outer halo regions. The dot-dashed curves in Figure 3 illustrate the Ludlow et al. (2011) model, assuming that $\gamma(r)$ follows an Einasto profile (Einasto 1965). The blue, green, and red dot-dashed lines correspond to $\alpha=0.230,\,0.178,\,$ and 0.132, respectively. Thus, we find that the Ludlow et al. (2011) expression accurately describes the shapes of Symphony $\beta(\gamma)$ profiles for $\gamma \gtrsim -2$, while we find systematically lower values of β in the outskirts. This comparison indicates that Symphony hosts are less relaxed than the Ludlow et al. (2011) halos from which Equation 5 was derived; note that we do not apply a relaxation cut to our host samples, which could partially explain this difference.

3.3 PPSD profiles

Figure 4 shows the mean measured radial PPSD profiles of simulated host halos at z=0 in each suite in the same format as Figure 2. In the left panel of Figure 4, the mean PPSD profiles from all simulation suites follow an almost identical power-law form, to remarkable precision, despite the fact that individual halos exhibit diverse density and velocity structures even at fixed mass. At face value, the slope

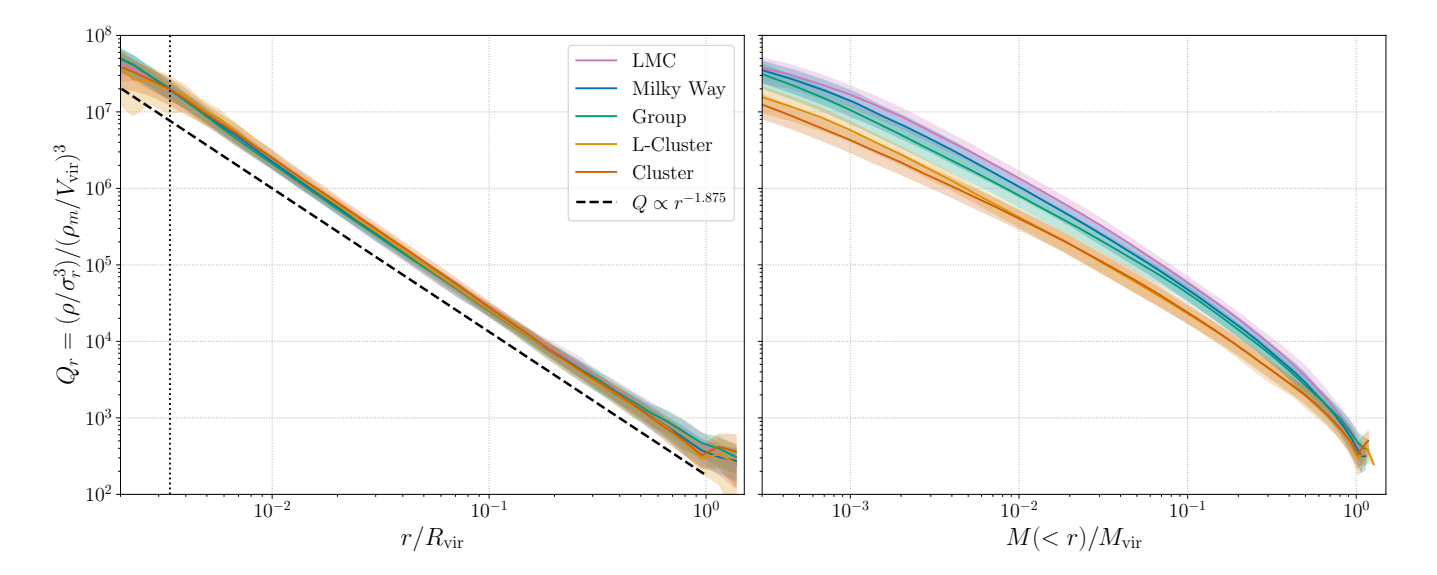


Figure 4. Left panel: Mean radial PPSD $\rho/\sigma_{\rm rad}^3$ profiles of Symphony host halos, normalized by $\rho_m/V_{\rm vir}^3$, as a function of radius in units of $R_{\rm vir}$ for each suite. Shaded regions denote the 68% halo-to-halo scatter. The dashed line represents the Bertschinger (1985) spherical secondary-infall similarity solution, $\rho/\sigma^3 \propto r^{-1.875}$. The dotted vertical line marks the most conservative convergence radius across suites. Right panel: Same as the left panel, but shown as a function of enclosed mass normalized by the host virial mass $M_{\rm vir}$.

of this universal power-law strikingly resembles the self-similar solution $\rho/\sigma^3 \propto r^{-1.875}$ (dashed line), as predicted by spherical secondary infall models (Bertschinger 1985). This apparent power-law behavior has also been identified in previous cosmological *N*-body simulations (e.g., Taylor & Navarro 2001; Dehnen & McLaughlin 2005; Navarro et al. 2010; Ludlow et al. 2010a, 2011).

However, as we will demonstrate, PPSD profiles systematically deviate from a universal power law in a way that correlates with the host halo's dynamical state. One aspect of this non-universality is shown in the right panel of Figure 4, where we plot the same mean PPSD profiles but as a function of enclosed mass, $M(< r)/M_{\rm vir}$ (i.e., using Lagrangian coordinates), rather than as a function of radius (i.e., using Eulerian coordinates). Unlike the radial profiles, the PPSD noticeably deviates from a power law when plotted as a function of enclosed mass.

The PPSD mass profiles reveal a systematic deviation between the lower-mass (LMC, Milky-Way, and Group) and higher-mass (L-Cluster and Cluster) *Symphony* suites. This separation likely arises due to significant differences in host halo density and velocity dispersion profiles between the lower-mass and higher-mass suites, which are apparent in Figure 2. Nadler et al. (2023) show that these groups of *Symphony* suites also differ in terms of their underlying host halo mass accretion histories (MAHs), which are known to correlate with halo density profiles (e.g., Dalal et al. 2010; Ludlow et al. 2013).

We understand the difference between PPSD profiles as a function of radius and enclosed mass in Figure 4 as follows. When plotting PPSD profiles in Eulerian coordinates (i.e., as a function of radius), dynamical relaxation processes such as phase mixing and violent relaxation tend to smooth out profile differences to produce more universal behavior; in other words, a given radius generally contains contributions from multiple overlapping mass shells that have crossed and mixed during halo evolution. However, when plotting PPSD profiles in Lagrangian coordinates (i.e., as a function of enclosed mass), each mass shell retains memory of its specific accretion and collapse history, making the PPSD profile more sensitive to detailed differences in hosts' MAHs.

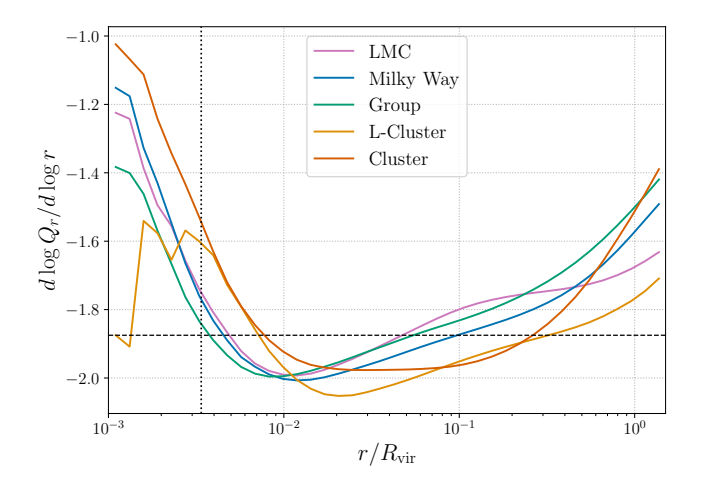


Figure 5. Mean logarithmic slope of PPSD profiles of host halos in *Symphony* suites at z=0. The dashed line marks the universal relation $Q_r \propto r^{-1.875}$. The dotted vertical line marks the most conservative convergence radius across the suites.

Figure 5 shows the logarithmic slope of the PPSD profiles as a function of radius for each suite, compared to the single power-law behavior predicted by the secondary infall model of Bertschinger (1985), $Q_r \propto r^{-1.875}$. We find that the PPSD profiles for each suite do not follow an exact power law, but tend to be shallower than -1.875 in the innermost and outermost regions, and steeper than -1.875 in the intermediate range, $0.01R_{\rm vir} \lesssim r \lesssim 0.1R_{\rm vir}$. Interestingly, these PPSD slope profiles are much largely independent of suite mass, which suggests that halos of different masses have similar PPSD shapes.

The behavior in Figure 5 is consistent with previous simulation results (e.g., Vass et al. 2009a; Navarro et al. 2010; Ludlow et al. 2010a, 2011) and indicates that PPSD profiles systematically deviate

from a universal power law; as discussed above, this departure from a power law is even more severe as a function of enclosed mass. This non-universal behavior is consistent with the results of Nadler et al. (2017), who used fluid simulations to show that the PPSD does not follow a universal power law as a function of either enclosed mass or radius (also see Arora & Williams 2020). In the following section, we study the origins of this non-universal behavior.

4 NON-UNIVERSALITY OF PPSD PROFILES

4.1 Deviation from Jeans Equilibrium

Spherically symmetric dark matter halos in equilibrium satisfy the Jeans equation:

$$\frac{\mathrm{d}}{\mathrm{d}r} \left[\rho(r) \,\sigma_{\mathrm{rad}}^2(r) \right] + \frac{2\beta(r)}{r} \,\rho(r) \,\sigma_{\mathrm{rad}}^2(r) = -\rho(r) \,\frac{\mathrm{d}\Phi(r)}{\mathrm{d}r},\tag{6}$$

where $\rho(r)$ is the density profile, $\sigma_{\rm rad}(r)$ the radial velocity dispersion, $\beta(r)$ the velocity anisotropy parameter, and $\Phi(r)$ the gravitational potential. In general, this equilibrium condition is not exactly satisfied by realistic halos formed in N-body simulations. To quantify the degree to which halos deviate from Jeans equilibrium, we define the *Jeans deviation parameter* $\delta_I(r)$ as

$$\delta_{J}(r) \equiv \left| \frac{\frac{\mathrm{d}}{\mathrm{d}r} \left[\rho(r) \, \sigma_{\mathrm{rad}}^{2}(r) \right] + \frac{2\beta(r)}{r} \, \rho(r) \, \sigma_{\mathrm{rad}}^{2}(r) + \rho(r) \, \frac{\mathrm{d}\Phi(r)}{\mathrm{d}r}}{\rho(r) \, \frac{\mathrm{d}\Phi(r)}{\mathrm{d}r}} \right|. \tag{7}$$

This dimensionless quantity measures the local imbalance between the pressure gradient and the gravitational force. ² By construction, a halo in perfect Jeans equilibrium at satisfies $\delta_J(r)=0$ at all radii, while larger values of $\delta_J(r)$ indicate stronger departures from equilibrium.

To assess the global level of disequilibrium within a halo, we define a *total Jeans deviation parameter* δ_I as:

$$\delta_J \equiv \int_0^{R_{\text{vir}}} \delta_J(r) \, dr,\tag{8}$$

where R_{vir} is the virial radius. In Appendix B, we demonstrate that this integrated quantity provides a consistent measure of the overall departure from equilibrium and correlates well with the commonly-used virial ratio $\eta = 2|K|/U$, where K and U respectively denote the total kinetic and potential energy.

4.2 Jeans deviation drives PPSD non-universality

We show the relation between the total Jeans deviation parameter δ_J and the best-fit PPSD slope in the left panel of Figure 6. The dashed line denotes the single power-law behavior predicted by the Bertschinger (1985) secondary infall model, $Q_r \propto r^{-1.875}$. To remove the mass dependence of δ_J among halos within each simulation suite, the right panel shows PPSD slope versus the Jeans deviation normalized within each suite,

$$\delta_{J,\text{norm}} \equiv \frac{\delta_J - \delta_{J,\text{med}}}{\sigma_{\delta_J}},\tag{9}$$

where $\delta_{J,\mathrm{med}}$ and σ_{δ_J} denote the median and standard deviation of δ_J within the corresponding suite, respectively. Note that the Cluster suite is excluded in this figure, since its $\delta_{J,\mathrm{norm}}$ distribution significantly differs from the other suites (see Appendix C). However, our results do not qualitatively change if the Cluster suite is included in the following analyses.

Figure 6 shows that halos in different dynamical states can significantly deviate from the self-similar prediction. In particular, some halos exhibit average PPSD slopes shallower than -1.7 or steeper than -2.0. More interestingly, we find a clear systematic trend: the farther a halo deviates from equilibrium (i.e., the larger δ_J), the steeper its average PPSD slope becomes. The correlation between best-fit PPSD slope and normalized Jeans deviation is highly significant according to a Spearman correlation test ($\rho = -0.387$, $p = 3.17 \times 10^{-8}$). Thus, the strong correlation shown in the left panel of Figure 6 is not purely driven by host halo mass. Note that these correlations remain strong and significant under jack-knife resampling, indicating that they are not driven by outlier hosts with large δ_J or $\delta_{J,\text{norm}}$.

Based on this result, we suggest that the canonical relation $Q \propto r^{-1.875}$ observed in earlier *N*-body studies arises primarily from averaging halos across a range of dynamical states, and that a halo's PPSD values strongly correlates with its departure from Jeans equilibrium. This echoes the findings of Nadler et al. (2017), which we will discuss below. We note that hints of this correlation between disequilibrium and PPSD slope have appeared in previous work. For example, Ludlow et al. (2010a) and Ludlow et al. (2011) suggested that deviations from a power law may reflect the presence of substructure or halo asphericity, both of which are known to indicate disequilibrium. Our finding that PPSD slopes correlate with departures from Jeans equilibrium provides a physical interpretation for these results.

4.3 Evolution of non-universal PPSD profiles

Next, we consider how the PPSD slopes changes with radius and redshift. We divide the *Symphony* host halos (again excluding the Cluster suite) into quartiles according to their normalized Jeans deviation parameter. The mean PPSD slope profile for each quartile is shown in Figure 7. The first noticeable feature is that the more relaxed halos systematically exhibit shallower PPSD slopes compared to those that are further from equilibrium, consistent with the trends discussed above.

In addition, the PPSD slope noticeably differs between radial regions. In the outer halo, the PPSD slopes display large scatter across different hosts, whereas in the inner region, the slopes are much less sensitive to the Jeans deviation parameter and tend to converge toward a nearly universal value of ~ -2.0 . This behavior indicates that more dynamically relaxed regions within halos tend to develop more self-similar and universal PPSD profiles.

To clarify the origin of the PPSD shapes presented in Figure 7 and to track their redshift evolution, Figure 8 shows the mean PPSD slope and the halo-to-halo scatter over time, as measured in comoving coordinates.³ The PPSD retains an approximately power-law form, $Q(r) \propto r^{-1.875}$, with the same characteristic trend of being steeper in the inner halo and flatter in the outer halo, persisting back to at least z=3. This is qualitatively consistent with earlier findings (e.g., Hoffman et al. 2007), who reported a PPSD power-law index

Note that, because we use an absolute value in Equation 7, our Jeans deviation parameter does not distinguish between "pressure-driven" versus "gravitation-driven" departures from Jeans equilibrium.

³ We exclude both the L-Cluster and Cluster suites for this analysis, since their mass accretion histories differ significantly from the other suites (Nadler et al. 2023); again, this choice does not qualitatively affect our results.

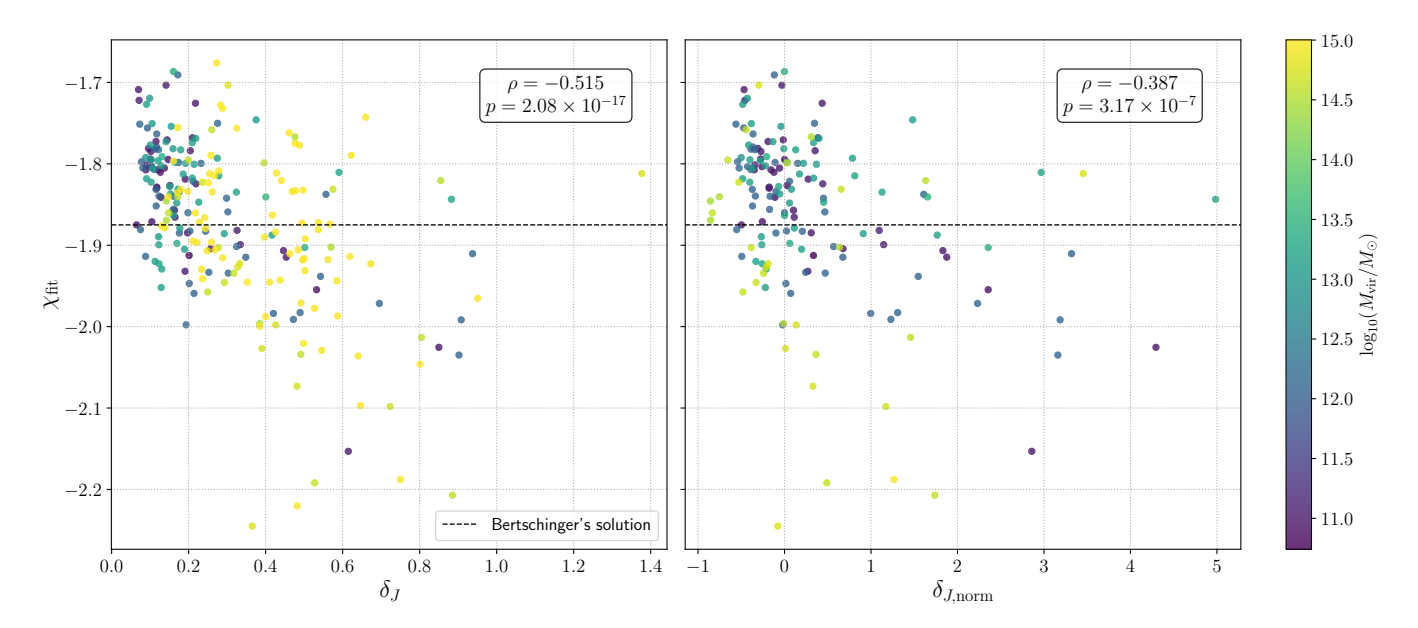


Figure 6. Left panel: Best-fit logarithmic slope of radial PPSD profiles versus total Jeans deviation (Equation 8). The dashed line marks the universal relation $Q_r \propto r^{-1.875}$. The upper legend lists the Spearman correlation coefficient, which implies that hosts with larger δ_J systematically develop steeper PPSD slope. Right panel: The same as the left panel but we normalize δ_J to $\delta_{J,\text{norm}}$ (Equation 9) to remove the dependence on halo mass. Note that this panel excludes the Cluster suite as described in the text.

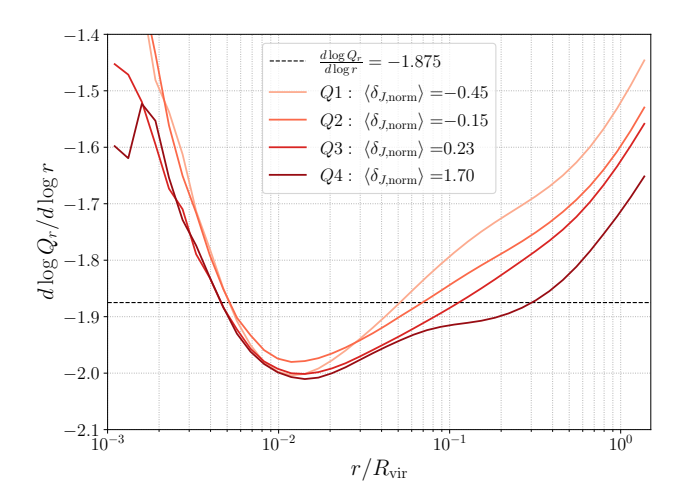


Figure 7. Mean radial profiles (solid lines) of the radial PPSD slope for *Symphony* host halos at z=0 (excluding the Cluster suite), split within each suite into quartiles of the normalized Jeans deviation, $\delta_{J,\text{norm}}$. QI corresponds to the most relaxed halos, while Q4 represents the most disturbed systems. The legend shows the mean normalized Jeans deviation for each quartile and the dashed line represents the universal relation $Q_r \propto r^{-1.875}$.

near -1.9. However, with a substantially larger halo sample, we demonstrate robustly that the best-fit PPSD slope is steeper at higher redshifts (left panel of Figure 8). Furthermore, the right panel of Figure 8 shows that the halo-to-halo scatter of the PPSD slope shrinks to small values in the inner region by z=0, while the halo-to-halo scatter is significantly larger in halo outskirts. These trends indicate that the inner PPSD is better approximated by a universal power law (albeit with an index somewhat steeper than -1.875), whereas PPSD profiles in the outer regions are less universal.

The behavior shown in Figure 8 can again be understood in terms of

deviations from Jeans equilibrium. Figure 9 shows the redshift evolution of the Jeans deviation parameter: halos undergo rapid mass growth and frequent major mergers at high redshift, so their inner regions form and relax earlier while the outer regions continue to evolve. As a result, the radial and redshift-dependent scatter of the PPSD slope closely follows the evolution of the Jeans deviation, such that larger departures from equilibrium correspond to greater nonuniversality and systematically steeper PPSD slopes. This connection provides a natural explanation for why ensemble averages over halos at different dynamical stages yield a power-law PPSD scaling, even though individual halos may deviate substantially from this relation. Note that this argument only predicts that a power-law slope approximately emerges, but the specific *value* of the power-law index does not have a deep physical significance in this picture. Thus, we interpret the value of the averaged PPSD slope (and the canonical -1.875 slope that is often reported) as a coincidence of averaging over halos in different dynamical states.

4.4 Correlations with halos secondary properties

Figures 10 and 11 present correlations between the best-fit PPSD slope and two key secondary halo properties: the virial concentration, defined as $c \equiv r_{\rm vir}/r_s$, and the dynamical accretion rate,

$$\Gamma(\Delta t_{\rm dyn}) \equiv \frac{M_{\rm vir}(t_0) - M_{\rm vir}(t_0 - t_{\rm dyn})}{t_{\rm dvn}}, \tag{10}$$

both measured at z = 0, where $t_{\rm dyn}$ denotes the halo dynamical time. As in Figure 6, the left panels of these figures show the relation using raw secondary halo properties. To remove any residual mass dependence, the right panels use versions of these secondary halo properties normalized within each simulation suite, following the same procedure as in Equation 9. For these figures, we include all suites since the normalized concentration and accretion rate distributions are statistically consistent across suites (see Appendix C).

Figures 10 and 11 reveal that the best-fit average PPSD slope

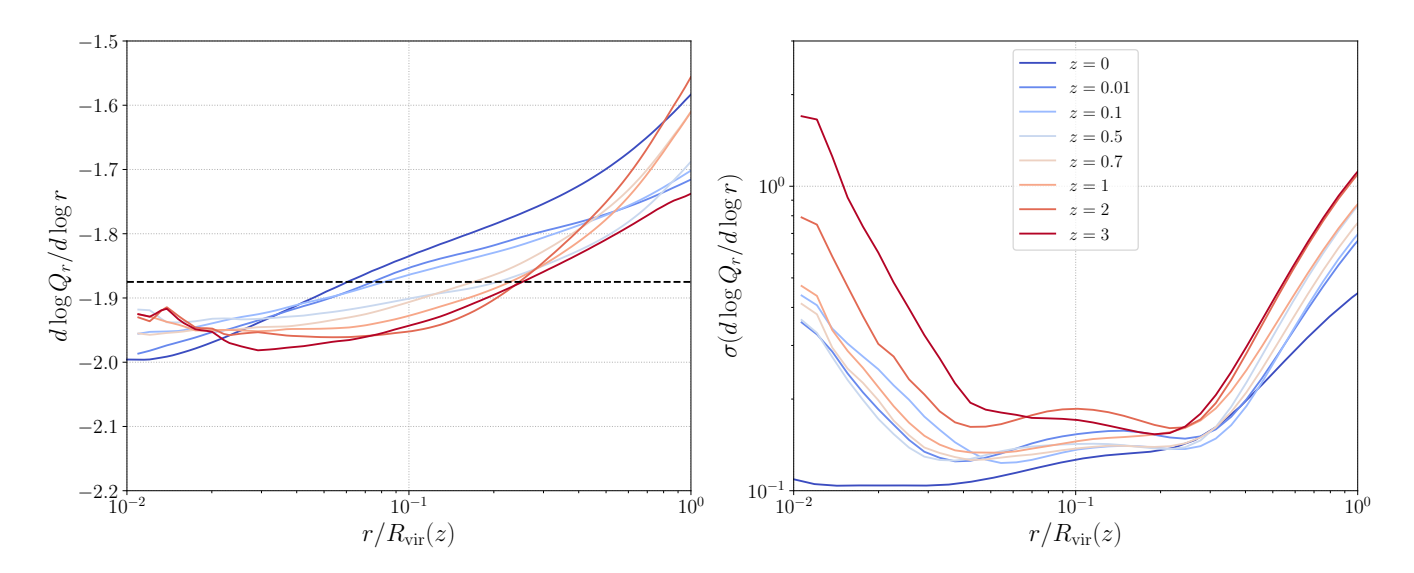


Figure 8. Evolution of the radial PPSD slope for host halos in LMC, Milky-Way and Group suites. *Left panel*: Mean logarithmic slope of Q_r as a function of radius in units of $R_{\text{vir}}(z)$ at different redshifts. The dashed line indicates the canonical -1.875 slope for reference. *Right panel*: Radial profile of the standard deviation of the PPSD slope across all host halos, which reveals the extent to which PPSD profiles differ from halo to halo as a function of radius and redshift.

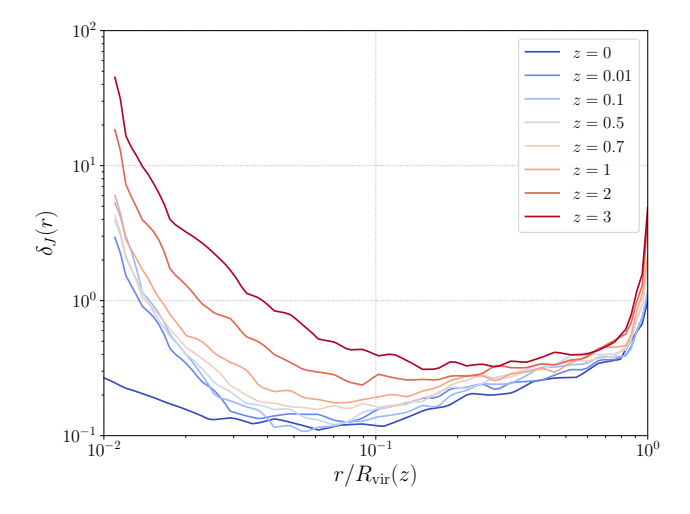


Figure 9. Average radial profiles of the Jeans deviation parameter, $\delta_J(r)$, for the LMC, Milky-Way, and Group suites shown in Figure 8, as a function of redshift. Radii are scaled by each halo's virial radius at the corresponding snapshot, and the profiles are averaged over all suites at each redshift.

systematically depends on both concentration and accretion rate. More concentrated halos tend to display shallower PPSD slopes, whereas halos experiencing more intense accretion show systematically steeper slopes, even when using normalized accretion rates ($\rho=0.19,\ p=3.37\times10^{-3}$, Spearman test). Moreover, the correlation with normalized accretion rate is substantially stronger than that with normalized concentration ($\rho=-0.386,\ p=4.26\times10^{-9}$, Spearman test), suggesting that the shape of the PPSD profile correlates most strongly with recent mass accretion history.

These trends reinforce the physical connection between the PPSD slope and the degree of dynamical equilibrium quantified by the Jeans deviation parameter. Concentration and accretion rate are both indirect tracers of a halo's dynamical state: halos with higher con-

centrations typically complete their major assembly earlier and thus are more dynamically relaxed, leading to smaller δ_J values and shallower PPSD slopes. In contrast, halos with higher accretion rates are dynamically younger and further from equilibrium, yielding larger δ_J values and correspondingly steeper PPSD slopes. Therefore, the correlations between the PPSD slope and secondary halo properties like concentration and accretion rate can be understood as manifestations of the more fundamental relationship between the PPSD profile shape and the halo's deviation from Jeans equilibrium.

5 COMPARISON TO THE 1D FLUID COLLAPSE SIMULATION

For a monatomic ideal gas, the local specific entropy (i.e., entropy per particle) can be expressed as

$$s_{\rm gas}(r) = -k_{\rm B} \ln K_{\rm gas}^{3/2}(r) + \text{constant}, \tag{11}$$

where $k_{\rm B}$ is the Boltzmann constant. The quantity $K_{\rm gas}$ denotes the conventional "entropy" of the intracluster medium (ICM) widely used in X-ray observations, defined as

$$K_{\rm gas} \equiv \frac{3k_{\rm B}T_{\rm g}}{\mu m_{\rm p}} \rho_{\rm g}^{-2/3} = \sigma_{\rm g}^2 \, \rho_{\rm g}^{-2/3},$$
 (12)

where $T_{\rm g}$, $\rho_{\rm g}$, and $\sigma_{\rm g}$ are the gas temperature, density, and velocity dispersion, respectively, and $\mu m_{\rm p}$ is the mean particle mass (Dalcanton & Hogan 2001).

Equation 12 provides a natural analogue for defining the thermodynamic entropy of a collisionless dark matter (DM) system (Faltenbacher et al. 2007),

$$K_{\rm DM} \equiv \sigma_{\rm DM}^2 \rho_{\rm DM}^{-2/3} = Q^{-2/3}$$
. (13)

Both numerical simulations and X-ray observations of galaxy clusters have shown that the gas entropy and dark matter PPSD respectively follow a radial scaling of $K \propto r^{1.2}$ and $Q \propto r^{-1.8}$, supporting this correspondence (e.g., Faltenbacher et al. 2007; Cavagnolo et al. 2009a;

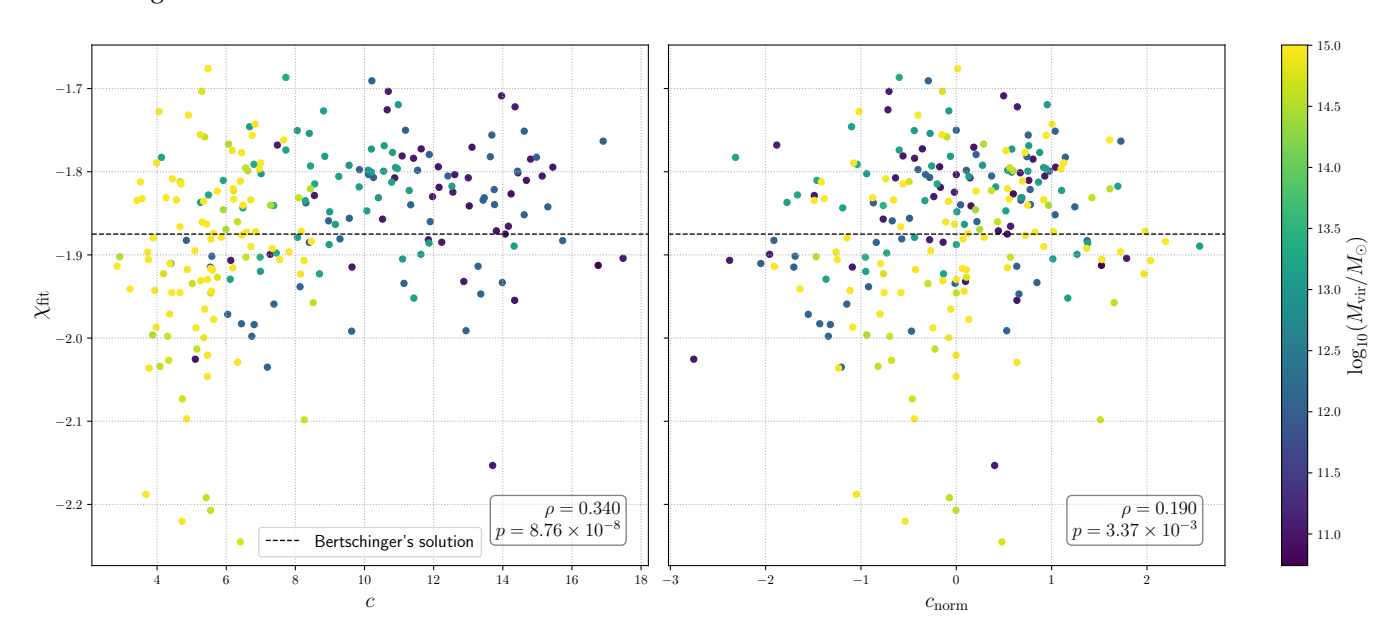


Figure 10. Left panel: Best-fit logarithmic slope of radial PPSD profiles versus host halo's concentration at z=0 for all Symphony suites. The dashed line represents the universal relation $Q_r \propto r^{-1.875}$. Right panel: The same as the left panel but we normalize concentration within each suite to remove the mass trend.

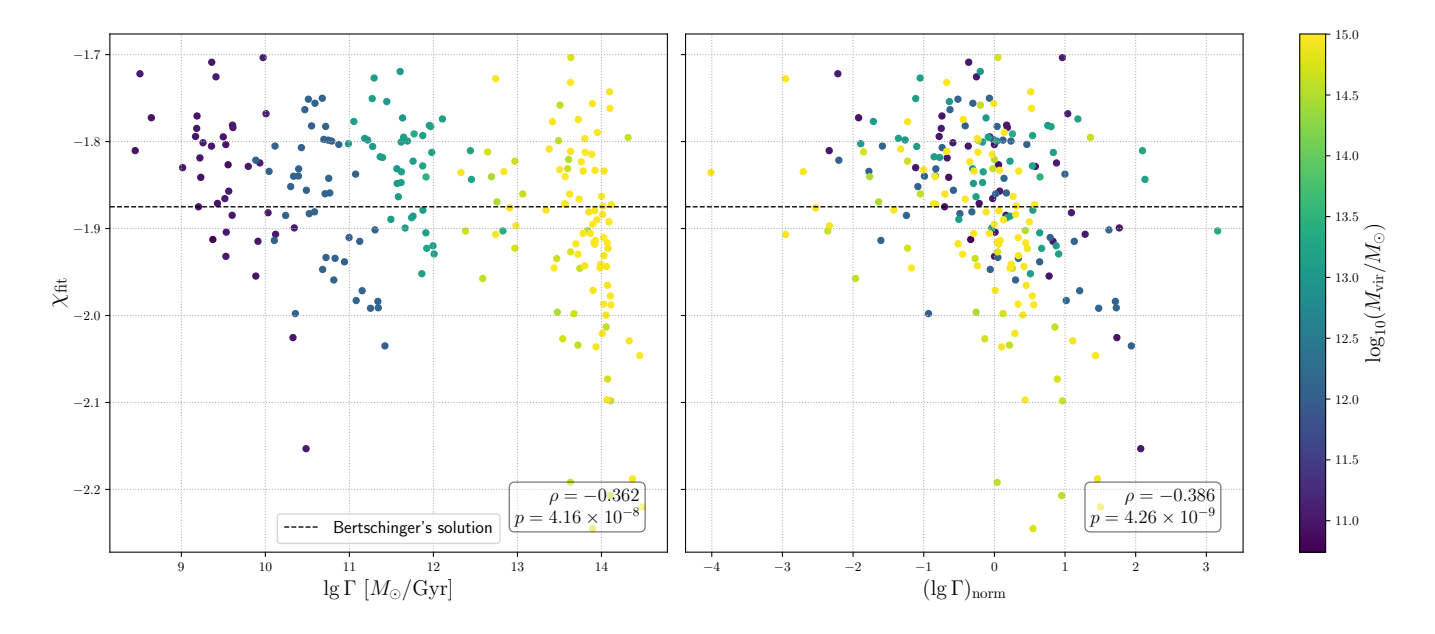


Figure 11. Left panel: Best-fit logarithmic slope of radial PPSD profiles versus dynamical accretion rate at z = 0 for all Symphony hosts. The dashed line shows the universal relation $Q_r \propto r^{-1.875}$. Right panel: The same as the left panel but with concentration normalized within each suite to remove the mass trend.

Capasso et al. 2019; Marini et al. 2020). This empirical similarity suggests that the thermodynamic structuring of hot gas and the dynamical relaxation of dark matter are governed by analogous physical principles.

Following this connection, Nadler et al. (2017) employed a fluid approximation to investigate deviations from the idealized power-law

⁴ For ICM gas in observed galaxy clusters, the entropy profile can be flattened in the inner regions due to AGN feedback and radiative cooling, but follows a power law at large radii where such effects become negligible (e.g., Cavagnolo et al. 2009a).

PPSD (or entropy) profile. Figure 12 compares our simulation results with their 1D hydrodynamic simulation predictions that employ a realistic halo mass accretion history (i.e., the blue line in Figure 10 of Nadler et al. 2017). We compare as a function of enclosed mass rather than radius because the Nadler et al. (2017) radial profiles are normalized to the shock radius in their hydrodynamic simulations, which is not well defined in our N-body halos.

The residuals of our radial entropy measurement agree remarkably well with the Nadler et al. (2017) prediction, indicating that onedimensional fluid simulations accurately reproduce entropy (and thus PPSD) power-law deviations found in our three-dimensional cosmo-

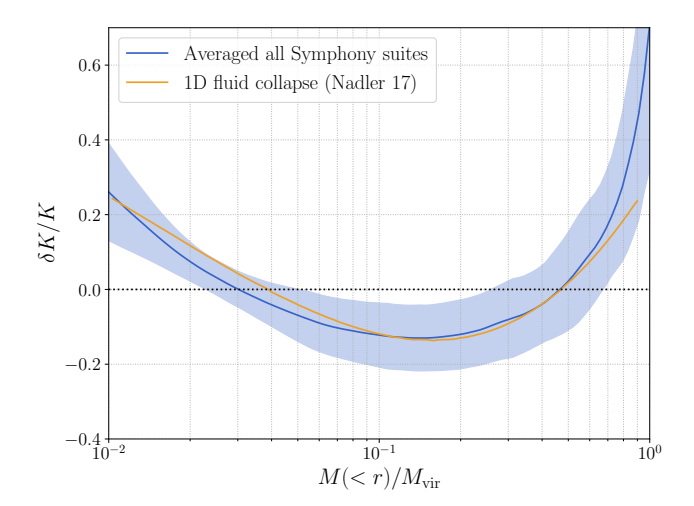


Figure 12. Stacked residuals of the entropy profile of Symphony host halos relative to power-law fits, compared with the 1D realistic fluid collapse model of Nadler et al. (2017). The residuals, $(K_{\rm fit}-K)/K$ with $K=Q_r^{2/3}$, are shown as a function of enclosed mass $M(< r)/M_{\rm vir}$ for all Symphony host halos. The shaded band denotes the 1σ halo-to-halo scatter and the orange curve is the result of Nadler et al. (2017). The horizontal dashed line marks a perfect power-law entropy profile.

logical N-body zoom-in simulations. This correspondence implies that the shape of the PPSD and its deviation from a power law are primarily determined by departures from Jeans (or, in a fluid context, hydrostatic) equilibrium, as encoded in halo assembly history, consistent with the predictions in Nadler et al. (2017).

As a result, we conclude that three-dimensional dynamical effects such as velocity anisotropy and cosmological effects such as filamentary accretion only play a minor role in determining the PPSD. This conclusion is consistent with the fact that total and radial PPSD profiles are very similar in our simulations (Appendix A1). This similarity between total and radial PPSD profiles must hold given the close correspondence between our measurements and the fluid model predictions shown in Figure 12. Furthermore, these results suggest that the radial orbit instability (ROI) does not significantly affect the PPSD, consistent with the arguments in Nadler et al. (2017), despite the importance of the ROI in shaping halos' central density and velocity disperion profiles (e.g., MacMillan et al. 2006).

6 SUMMARY AND DISCUSSION

6.1 Main Findings

We analyzed the density, velocity dispersion, velocity anisotropy, and pseudo-phase-space density (PPSD) profiles of 246 host halos spanning five mass decades from the *Symphony* simulation suite. We investigated how the PPSD profiles deviate from the previously reported universal power law relation and explored how these deviations correlate with the degree of dynamical equilibrium, mass accretion history, and other secondary halo properties.

Our main findings are as follows:

• PPSD profiles do not exactly follow a universal power law. In particular, Symphony hosts' PPSD profiles systematically deviate from the canonical $Q \propto r^{-1.875}$ power law. Across all suites, the logarithmic slope of Q(r) is steeper than -1.875 in the inner regions $(r/R_{\rm vir} \lesssim 10^{-1})$ and shallower at larger radii (Figure 5).

- Halos farther from Jeans equilibrium exhibit steeper average PPSD slopes. Halos that deviate more strongly from Jeans equilibrium, as quantified by our Jeans deviation parameter (Equation 7), have significantly steeper average PPSD slopes (Figure 6). This correlation remains highly significant, even after controlling for halo mass and performing jackknife resampling.
- Halo mass assembly histories shape PPSD profiles. The average PPSD slope is steep (close to -2.0) in the inner halo $(r/R_{\rm vir} \lesssim 10^{-1})$ and becomes increasingly stable toward lower redshifts. At larger radii, however, the slope exhibits substantial halo-to-halo scatter that persists until the present day (Figure 8). This behavior reflects halo assembly: rapid accretion and mergers at early times drive strong departures from Jeans equilibrium and produce the large variability in outer PPSD slopes, whereas subsequent relaxation leads to the convergence toward a more universal inner profile.
- PPSD profiles depend on halo concentration and accretion rate. The best-fit average PPSD slopes show a weak but systematic correlation with concentration and a much stronger correlation with recent accretion rate: more concentrated (and thus dynamically older) halos tend to have slightly shallower slopes, whereas rapidly accreting halos exhibit significantly steeper slopes (Figures 10–11). These trends persist after controlling for host halo mass.
- 1D self-similar fluid collapse model largely recovers the shape of PPSD profiles in N-body simulations. The PPSD profiles measured in our simulations are in remarkable agreement with predictions from the Nadler et al. (2017) one-dimensional fluid model (Figure 12). Deviations from the ideal power-law PPSD can therefore be explained by departures from Jeans equilibrium, which are ultimately set by halo assembly history alone.

Thus, we argue that a power-law PPSD approximately emerges from ensemble averaging over halos in different dynamical states, and that PPSD profiles deviate from a universal power-law relation because they encode halos' diverse mass assembly histories and dynamical states. In this picture, the PPSD is primarily governed by quasi-hydrostatic relaxation rather than three-dimensional effects such as velocity anisotropy or cosmological effects such as filamentary accretion.

6.2 Outlook and Future Work

These results build on previous studies in several ways. For example, Nadler et al. (2017) found that the PPSD deviates from a universal power-law relation because of deviations from hydrostatic equilibrium in their one-dimensional hydrodynamic simulations. Our results confirm this prediction in a three-dimensional cosmological setting without relying on the fluid approximation. Moreover, the striking similarity between our PPSD profile and the (appropriately transformed) Nadler et al. (2017) gas entropy profile (Figure 12) suggests that the PPSD is primarily determined by halo mass assembly history, clarifying the interpretation of the Nadler et al. (2017) results. Meanwhile, Arora & Williams (2020) argued that a power-law PPSD is not a fundamental outcome of gravitational evolution based on the structure of the Jeans equation, even for equilibrium halos. Our results strengthen this conclusion for non-equilibrium halos.

Our results are based on *Symphony* CDM simulations with fixed cosmological parameters within each suite, raising the question of how the PPSD behaves in other cosmologies. For example, Brown et al. (2020) found that PPSD is sensitive to the shape of the primordial matter power spectrum and that the apparent universality of PPSD profiles may result from the fairly narrow range of initial

conditions used in most cosmological simulations. Our key result that halo mass assembly history determines the PPSD implies that variations in the PPSD are *determined* by the impact of these initial conditions on halo mass assembly histories. This is plausible, since mass assembly histories reflect the initial conditions for structure formation (e.g., Lu et al. 2006). A dedicated study is needed to test whether our prediction is consistent with the Brown et al. (2020) results

In a similar vein, our framework can be used to understand the PPSD in dark matter models beyond CDM. For example, in models that alter the initial conditions for structure formation like warm dark matter (WDM), we predict that changes to the PPSD relative to CDM will be determined by the impact of power spectrum suppression on halo growth histories. This is a timely area for future work given previous studies on the WDM PPSD (e.g., Dalcanton & Hogan 2001; Macciò et al. 2012; Shao et al. 2013) as well as the large suites of WDM simulations now available (e.g., Rose et al. 2025; Nadler et al. 2025a). Non-gravitational dark matter physics can also alter the PPSD. For example, self-interacting dark matter (SIDM) models produce central cores in density and velocity dispersion profiles, leading to a cored inner PPSD (e.g., Rocha et al. 2013; Chua et al. 2021). It will also be interesting to revisit the PPSD in modern SIDM simulations, which adopt high-amplitude, velocity-dependent cross sections and produce both core formation and collapse (e.g., Nadler et al. 2025b).

Finally, we note that studying the PPSD and its evolution in subhalos is particularly interesting in light of our results, since subhalos deviate even more substantially from Jeans equilibrium than isolated halos during orbital evolution. For example, Vass et al. (2009b) found that the amplitude of the coarse-grained distribution function f (and thus of the PPSD) is orders-of-magnitude higher at the centers of subhalos compared to the main halo because this relatively unmixed material better captures the high primordial dark matter phase-space density at high redshifts. This high amplitude of the PPSD in subhalos is hinted at in Figure 1 and raises the question of how strongly our hosts' PPSD profiles are impacted by subhalos, similar to previous work for halo density profiles (e.g., Fielder et al. 2020). We expect that analyses of higher-resolution Symphony resimulations combined with recent analytic techniques for evolving subhalo phase-space distributions (e.g., Drakos et al. 2017) will shed light on these issues.

ACKNOWLEDGEMENTS

We thank Fangzhou Jiang, Phil Mansfield, and Jorge Peñarrubia for helpful discussions related to this work. This work used data from the *Symphony* suite of simulations, which were supported by the Kavli Institute for Particle Astrophysics and Cosmology at Stanford University and SLAC National Accelerator Laboratory, and by the U.S. Department of Energy under contract number DE-AC02-76SF00515 to SLAC National Accelerator Laboratory. S.P.O. acknowledges NSF AST-240752 for support.

DATA AVAILABILITY

Our analysis code is publicly available at https://github.com/Bocheng-Feng/Symphony-PPSD. All *Symphony* data we used is hosted at http://web.stanford.edu/group/gfc/gfcsims.

REFERENCES

Allgood B., Flores R. A., Primack J. R., Kravtsov A. V., Wechsler R. H., Faltenbacher A., Bullock J. S., 2006, MNRAS, 367, 1781

Arora A., Williams L. L. R., 2020, ApJ, 893, 53

Bertschinger E., 1985, ApJS, 58, 39

Bhattacharyya J., Adhikari S., Banerjee A., More S., Kumar A., Nadler E. O., Chatterjee S., 2022, The Astrophysical Journal, 932, 30

Binney J., Tremaine S., 2008, Galactic Dynamics: Second Edition

Biviano A., Mamon G. A., 2023, Astronomy & Samp; Astrophysics, 670, A17
Brown S. T., McCarthy I. G., Diemer B., Font A. S., Stafford S. G., Pfeifer S., 2020, MNRAS, 495, 4994

Bryan G. L., Norman M. L., 1998, ApJ, 495, 80

Capasso R., et al., 2018, Monthly Notices of the Royal Astronomical Society, 482, 1043–1061

Capasso R., et al., 2019, MNRAS, 482, 1043

Journal Supplement Series, 182, 12-32

Cavagnolo K. W., Donahue M., Voit G. M., Sun M., 2009a, ApJS, 182, 12 Cavagnolo K. W., Donahue M., Voit G. M., Sun M., 2009b, The Astrophysical

Chua K. T. E., Dibert K., Vogelsberger M., Zavala J., 2021, MNRAS, 500, 1531

Cole S., Helly J., Frenk C. S., Parkinson H., 2008, MNRAS, 383, 546

Colombi S., 2021, Astronomy & Samp; Astrophysics, 647, A66

Dalal N., Lithwick Y., Kuhlen M., 2010, The Origin of Dark Matter Halo Profiles (arXiv:1010.2539), https://arxiv.org/abs/1010.2539

Dalcanton J. J., Hogan C. J., 2001, The Astrophysical Journal, 561, 35-45

Dehnen W., McLaughlin D. E., 2005, MNRAS, 363, 1057

Drakos N. E., Taylor J. E., Benson A. J., 2017, MNRAS, 468, 2345

Dutton A. A., Macciò A. V., 2014, Monthly Notices of the Royal Astronomical Society, 441, 3359–3374

Einasto J., 1965, Trudy Astrofizicheskogo Instituta Alma-Ata, 5, 87

Faltenbacher A., Hoffman Y., Gottlober S., Yepes G., 2007, Monthly Notices of the Royal Astronomical Society, 376, 1327–1334

Fielder C. E., Mao Y.-Y., Zentner A. R., Newman J. A., Wu H.-Y., Wechsler R. H., 2020, MNRAS, 499, 2426

Gao L., Navarro J. F., Cole S., Frenk C. S., White S. D. M., Springel V., Jenkins A., Neto A. F., 2008, Monthly Notices of the Royal Astronomical Society, 387, 536–544

Hansen S. H., Moore B., 2006, New Astron., 11, 333

Hayashi E., White S. D. M., 2008, MNRAS, 388, 2

Hinshaw G., et al., 2013, The Astrophysical Journal Supplement Series, 208, 19

Hjorth J., Williams L. L. R., Wojtak R., McLaughlin M., 2015, The Astrophysical Journal, 811, 2

Hoffman Y., Romano-Diaz E., Shlosman I., Heller C., 2007, The Astrophysical Journal, 671, 1108–1114

Huss A., Jain B., Steinmetz M., 1999, The Astrophysical Journal, 517, 64–69 Lu Y., Mo H. J., Katz N., Weinberg M. D., 2006, MNRAS, 368, 1931

Ludlow A. D., Navarro J. F., Springel V., Vogelsberger M., Wang J., White S. D. M., Jenkins A., Frenk C. S., 2010a, MNRAS, 406, 137

Ludlow A. D., Navarro J. F., Springel V., Vogelsberger M., Wang J., White S. D. M., Jenkins A., Frenk C. S., 2010b, MNRAS, 406, 137

Ludlow A. D., Navarro J. F., White S. D. M., Boylan-Kolchin M., Springel V., Jenkins A., Frenk C. S., 2011, MNRAS, 415, 3895

Ludlow A. D., et al., 2013, Monthly Notices of the Royal Astronomical Society, 432, 1103–1113

Ludlow A. D., Navarro J. F., Angulo R. E., Boylan-Kolchin M., Springel V., Frenk C., White S. D. M., 2014, Monthly Notices of the Royal Astronomical Society, 441, 378–388

Ludlow A. D., Schaye J., Bower R., 2019, Monthly Notices of the Royal Astronomical Society, 488, 3663–3684

MacMillan J. D., Widrow L. M., Henriksen R. N., 2006, ApJ, 653, 43

Macciò A. V., Paduroiu S., Anderhalden D., Schneider A., Moore B., 2012, MNRAS, 424, 1105

Maciejewski M., Colombi S., Alard C., Bouchet F., Pichon C., 2009, Monthly Notices of the Royal Astronomical Society, 393, 703–722

Mandelbaum R., Seljak U., Hirata C. M., 2008, Journal of Cosmology and Astroparticle Physics, 2008, 006

- Mao Y.-Y., Williamson M., Wechsler R. H., 2015, The Astrophysical Journal, 810, 21
- Marini I., et al., 2020, Monthly Notices of the Royal Astronomical Society, 500, 3462–3480
- McBride J., Fakhouri O., Ma C.-P., 2009, Monthly Notices of the Royal Astronomical Society, 398, 1858–1868
- Merritt D., Navarro J. F., Ludlow A., Jenkins A., 2005, The Astrophysical Journal, 624, L85–L88
- Merritt D., Graham A., Moore B., Diemand J., Terzić B., 2006, The Astronomical Journal, 132, 2685–2700
- Nadler E. O., Oh S. P., Ji S., 2017, Monthly Notices of the Royal Astronomical Society, 470, 500–511
- Nadler E. O., et al., 2023, The Astrophysical Journal, 945, 159
- Nadler E. O., An R., Gluscevic V., Benson A., Du X., 2025a, ApJ, 986, 127
- Nadler E. O., Kong D., Yang D., Yu H.-B., 2025b, ApJ, 991, 69
- Navarro J. F., Frenk C. S., White S. D. M., 1996, ApJ, 462, 563
- Navarro J. F., Frenk C. S., White S. D. M., 1997, The Astrophysical Journal, 490, 493–508
- Navarro J. F., et al., 2004, Monthly Notices of the Royal Astronomical Society, 349, 1039–1051
- Navarro J. F., et al., 2009, Monthly Notices of the Royal Astronomical Society, 402, 21–34
- Navarro J. F., et al., 2010, MNRAS, 402, 21
- Neto A. F., et al., 2007, Mon. Not. Roy. Astron. Soc., 381, 1450
- Popolo A. D., 2011, Journal of Cosmology and Astroparticle Physics, 2011, 014–014
- Pratt G. W., Arnaud M., Pointecouteau E., 2006, Astronomy & Astrophysics, 446, 429–438
- Press W. H., Schechter P., 1974, ApJ, 187, 425
- Rocha M., Peter A. H. G., Bullock J. S., Kaplinghat M., Garrison-Kimmel S., Oñorbe J., Moustakas L. A., 2013, MNRAS, 430, 81
- Rose J. C., et al., 2025, ApJ, 982, 68
- Shao S., Gao L., Theuns T., Frenk C. S., 2013, MNRAS, 430, 2346
- Taylor J. E., Navarro J. F., 2001, ApJ, 563, 483
- Vass I. M., Valluri M., Kravtsov A. V., Kazantzidis S., 2009a, MNRAS, 395, 1225
- Vass I. M., Valluri M., Kravtsov A. V., Kazantzidis S., 2009b, MNRAS, 395, 1225
- Voit G. M., 2005, Reviews of Modern Physics, 77, 207-258
- Wang J., Bose S., Frenk C. S., Gao L., Jenkins A., Springel V., White S. D. M., 2020, Nature, 585, 39–42
- White S. D. M., Rees M. J., 1978, MNRAS, 183, 341
- Williams L. L. R., Austin C., Barnes E., Babul A., Dalcanton J., 2005, The phase-space density distribution of dark matter halos (arXiv:astro-ph/0412442), https://arxiv.org/abs/astro-ph/0412442
- Wu H.-Y., Hahn O., Wechsler R. H., Mao Y.-Y., Behroozi P. S., 2013a, The Astrophysical Journal, 763, 70
- Wu H.-Y., Hahn O., Wechsler R. H., Behroozi P. S., Mao Y.-Y., 2013b, The Astrophysical Journal, 767, 23
- Zavala J., Frenk C. S., 2019, Galaxies, 7, 81
- van Breugel F., Nathan Kutz J., Brunton B. W., 2020, IEEE Access
- van Breugel F., Liu Y., Brunton B. W., Kutz J. N., 2022, Journal of Open Source Software, 7, 4078
- van den Bosch F. C., 2002, Monthly Notices of the Royal Astronomical Society, 331, 98-110

APPENDIX A: ALTERNATIVE PPSD MEASUREMENTS

A1 Total versus radial PPSD

The total and radial pseudo-phase-space densities (PPSDs) are related through the expression

$$\frac{Q_{\text{tot}}(r)}{Q_r(r)} = [3 - 2\beta(r)]^{-3/2},\tag{A1}$$

where $\beta(r)$ denotes the velocity anisotropy profile of the halo. Figure A1 compares the total PPSD with the radial one. We find that their overall shapes and slopes exhibit very similar behavior across all suites and that their ratio is consistent with Equation A1.

Thus, the arguments presented in the main text for the radial PPSD equally apply to the total PPSD. In particular, while the slope of the total PPSD tends to be slightly shallower than that of the radial PPSD, its correlations with the Jeans deviation and other halo properties remain robust.

A2 Dimensionful PPSD

Figure A2 presents the mean radial PPSD profiles for each simulation suite in physical units of M_{\odot} kpc⁻³ (km s⁻¹)⁻³, shown as functions of radius (left panel, in units of kpc) and enclosed mass (right panel, in units of M_{\odot}). We find that the amplitude A in the power-law model $Q = A(r/R_{\rm max})^{-\chi}$ correlates with host halo mass.⁵ In particular, the amplitude of the best-fitting single power-law model follows a clear scaling relation:

$$\lg A \approx (-1.20 \pm 0.01) \lg M_{\text{vir}} + (13.54 \pm 0.19),$$
 (A2)

where A represents the value of radial PPSD at $R_{\rm max}$, the radius where the circular velocity reaches its maximum and $M_{\rm vir}$ denotes the virial mass of the host halo, and uncertainties represent 1σ intervals about the best-fit parameters. This scaling is consistent with the trend proposed by Dalcanton & Hogan (2001), who argued that systems assembled through hierarchical structure formation obey $Q \sim M^{-1}$.

This scaling arises because systems that assemble at roughly constant spatial density must undergo proportional increases in both size and velocity dispersion to maintain virial equilibrium. This leads phase-space volume to increase more rapidly than total mass, resulting in a characteristic decline of the coarse-grained phase-space density with increasing mass, i.e., $Q \propto M^{-1}$. The relation thus represents the slowest possible decrease of Q with mass, corresponding to the most quiescent merger histories.

APPENDIX B: JEANS DEVIATION VERSUS VIRIAL RATIO

The dynamical equilibrium of dark matter halos can be characterized using several criteria, such as the substructure mass fraction, the offset between the center of mass and the potential minimum, and the virial ratio (e.g., Neto et al. 2007). In this work, we introduce the Jeans deviation parameter, defined in Equation 7, which provides a more direct measure of the degree to which a system satisfies the Jeans equilibrium condition. This quantity can be evaluated as a function of radius to quantify the local imbalance between pressure support and gravitational force.

To verify that the total Jeans deviation parameter captures a similar physical meaning as conventional equilibrium measures, we compare it to the commonly used virial ratio for each host halo in the *Symphony* simulations (Figure B1). The two quantities exhibit a strong and statistically significant correlation (Spearman coefficient $\rho=0.820$, $p<10^{-10}$), confirming that the total Jeans deviation parameter provides a reliable estimator of a halo's dynamical relaxation state. For reference, the majority of *Symphony* host halos satisfy the virial ratio criterion for relaxed halos adopted by Neto et al. (2007), i.e., $\eta<1.35$.

APPENDIX C: SUITE CONSISTENCY TESTS

Halo properties such as concentration, accretion rate, and the total Jeans deviation parameter are expected to depend weakly on halo mass (e.g., Mandelbaum et al. 2008, McBride et al. 2009, Ludlow et al. 2014). To isolate correlations with the PPSD slope, we have normalized these secondary halo properties in certain analyses using Equation 9. To verify this procedure, Figure C1 presents the distributions of the normalized concentration, accretion rate, and total Jeans deviation parameter for host halos in each Symphony suite. The normalized concentration (c_{norm}) and accretion rate (Γ_{norm}) show nearly identical distributions across all suites. Kolmogorov–Smirnov (KS) tests further confirm this consistency, with p-values greater than 0.05 for all pairwise suite comparisons.

In contrast, the distribution of the normalized Jeans deviation parameter ($\delta_{J,norm}$) in the Cluster suite differs significantly from the others, as indicated by the KS test and by its bimodal structure in Figure C1. This is not surprising, given the major recent accretion events that many hosts in our Cluster sample experience (Nadler et al. 2023); this analysis justifies our choice in Figure 6, to only include the LMC, Milky Way, Group, and L-Cluster suites.

APPENDIX D: SMOOTHING DERIVATIVE ALGORITHM

To assess the reliability of our slope measurement method, we perform a recovery test using mock PPSD profiles. Specifically, we construct Q_r profiles that follow an exact power-law relation $Q \propto r^{-1.875}$ and introduce statistical noise by Poisson-sampling the expected particle counts within each radial bin, matching the noise level of our simulations.

The left panel of Figure D1 presents 250 (close to the number of hosts in Symphony) such noisy realizations for an NFW halo with concentration c=10, while the right panel shows the mean recovered slope and its $\pm 1\sigma$ scatter, obtained using the constant_jerk variant of the Kalman smoothing algorithm. The yellow-shaded region indicates the "well-recovered window," defined as the radial range where the mean recovered slope deviates by less than 1% from -1.875 and the realization-to-realization scatter remains below the mean dispersion across all radii, corresponding to $6\times 10^{-3} < r/R_{\rm vir} < 1.1$. Throughout this work, we therefore restrict our slope fitting to this range to ensure noise-robust measurements.

This paper has been typeset from a T_EX/IAT_EX file prepared by the author.

⁵ In this relation, we normalize radii by $R_{\rm max}$, the radius from the center of each halo at which $V_{\rm max}$ is achieved, to remove residual mass dependence across our suites.

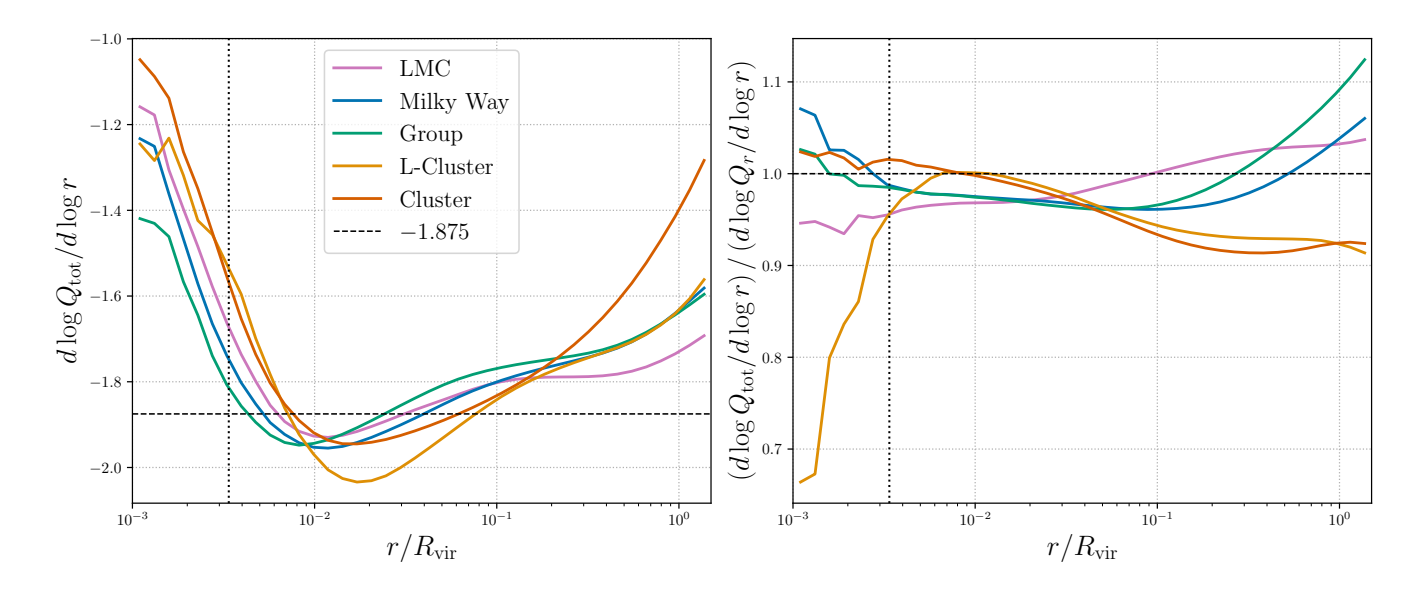


Figure A1. Left panel: Mean logarithmic slope of radial PPSD profiles of host halos in Symphony suites at z = 0. The dotted vertical line marks the most conservative convergence radius across all suites. Right panel: The ratio between total and radial PPSD slope profiles.

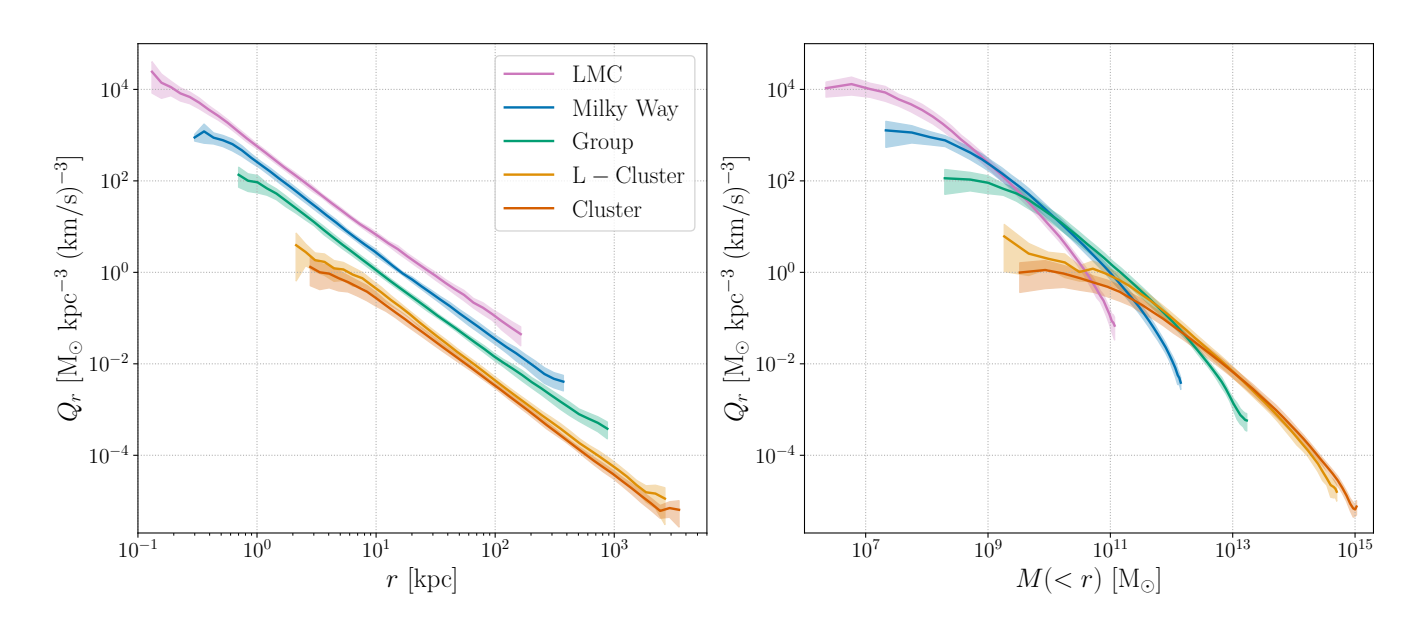


Figure A2. Same as Figure 4, but showing the dimensionful radial PPSD as a function of dimensionful radius (left panel) and dimensionful nclosed mass (right panel, in units of M_{\odot}).

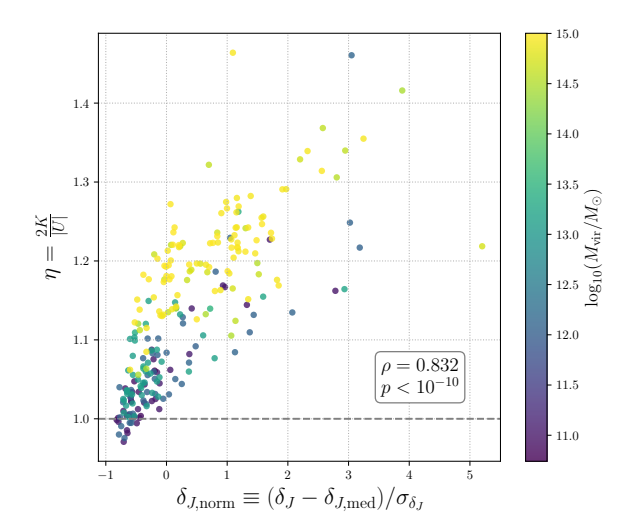


Figure B1. The relation between virial ratio and total normalized Jeans deviation parameter for host halos across all *Symphony* suites. The horizontal dashed line marks virial equilibrium and the legend lists the Spearman correlation coefficients.

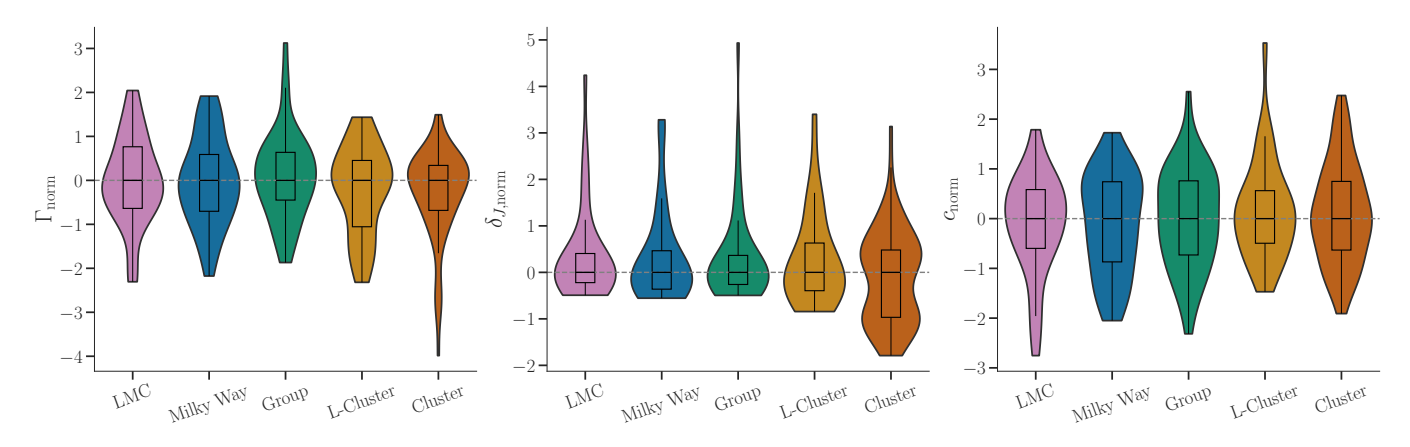


Figure C1. Violin and box plots of the normalized concentration, accretion rate, and total Jeans deviation parameter for host halos in each *Symphony* suite. Each distribution is normalized within its own suite following the manner of Equation 9, with violin shapes showing the full range and boxes indicating the interquartile ranges and medians.

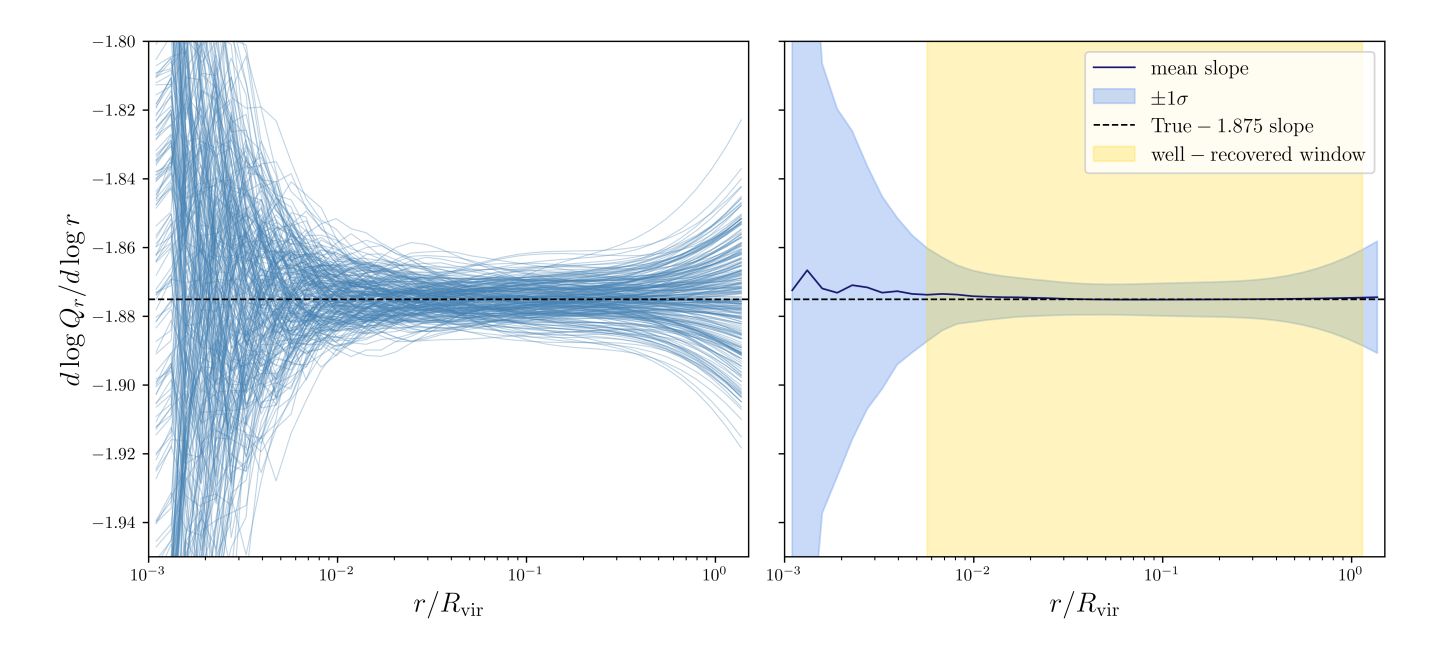


Figure D1. Recovery test of the PPSD slope using the constant_jerk Kalman smoothing method. The left panel shows 250 Poisson-noised realizations of mock NFW halos, and the right panel presents the mean recovered slope (solid line) with $\pm 1\sigma$ scatter (shaded). The dashed line marks the true slope, and the yellow band indicates the radial range where the slope is accurately recovered, spanning $6 \times 10^{-3} < r/R_{\rm vir} < 1.1$.